

WROCLAW UNIVERSITY OF TECHNOLOGY

MASTER'S THESIS

Electronic properties of graphene nanostructures

Author: Błażej Jaworowski

*Supervisor: prof. dr hab.
Arkadiusz Wójs*

*A thesis submitted in fulfilment of the requirements
for the degree of Master of Physics
in the Wrocław University of Technology*

July 2013



Politechnika Wrocławska

"The uses of Graphene seem limitless It truly deserves its dubbed name wonder sheet. Some ATS members have suggested that it has its origins from the Roswell incident due to various correlation such as date of Roswell incident coincide with Graphene being proposed. Both of these occurred in 1947. The description of the supposed debris from the Roswell UFO was metallic, light and if bent would flex back into shape."

- from an internet forum on conspiracy theories

Acknowledgements

I would like to thank my supervisor prof. Arkadiusz Wójs and Paweł Potasz for all the help and advice needed at all the stages of writing this thesis, and to Devrim Güçlü for introducing me into the Quantum Monte Carlo calculations.

The calculations in following work were performed on Supernova cluster at Wrocław Centre for Networking and Supercomputing.

Contents

Acknowledgements	ii
1 Introduction	1
2 Graphene as a crystal	3
2.1 Introduction	3
2.2 Crystal structure	5
2.3 Electronic structure	6
2.3.1 Tight-binding model	6
2.3.2 Dirac fermions	9
3 Graphene nanostructures	10
3.1 Experimental realization of graphene nanostructures	10
3.2 Edges of graphene	11
3.3 Edge and shape influence on electronic and magnetic properties	11
3.4 Nanoribbons	15
4 Disorder in graphene	16
4.1 Sources of disorder	16
4.2 Modelling disorder	17
4.3 Disorder and conductivity	18
4.4 Anderson disorder in graphene nanostructures	19
5 Methodology	21
5.1 The many-electron Hamiltonian	21
5.1.1 Hubbard model	22
5.2 Mean-field procedure for Hubbard model	22
5.3 Quantum Monte Carlo	25
5.3.1 Variational Monte Carlo	26
5.3.1.1 Idea of the method	26
5.3.1.2 Monte Carlo integration	26
5.3.1.3 Metropolis algorithm	27
5.3.1.4 Variance and MAD minimization using local energy	28
5.3.1.5 The form of the wave function	29
5.3.1.6 Cusp conditions	29
5.3.2 Diffusion Quantum Monte Carlo	31

*Dedicated to Saints and Madmen: Małgorzata S., Anna Frances
Caldwell, Katarzyna L., Wiktor B., Thérèse M., Jakub Ś. and others.*

Chapter 1

Introduction

In the story "The In-fall", written in 2010, a science fiction writer Ted Kosmatka describes a spaceship with a "graphene skin". While, in reality, graphene may be not the best material for constructing spaceships, it promises a bunch of scientific and technological breakthroughs. This is reflected in the growing interest in researching the physics of this material. Since 2004, when Geim and Novoselov took a piece of Scotch tape and used it to isolate the first graphene sample, the number of publications in this area is growing exponentially.

Why graphene is so interesting? The engineers (and probably the most of the laymen) are interested in the properties like the high electron mobility and great strength, which gives graphene a potential to revolutionize electronics. Scientists may be interested for example in the analogies between the Hamiltonian of electrons in graphene in low-energy approximation and the Dirac Hamiltonian in the 2D quantum electrodynamics. Although theoreticians had known it 20 years before the exfoliation of graphene, now they have the chance to see this in experiment.

Reducing the size of graphene samples to the nanoscale brings further extraordinary effects, namely the dependence of the electronic and magnetic properties on the shape of the sample. This means that one can have a ferromagnet, antiferromagnet or unpolarized structure from the same material, varying just the way of "cutting" it.

In this thesis, we perform two types of calculation referring to the properties of these nanofragments of graphene (also called "nanoflakes" or "graphene quantum dots"). First of all, we investigate how the presence of disorder, caused e.g. by interaction with substrate, changes the properties of the ideal system. We use the simple lattice models to capture the effect of disorder on electronic structure and stability of magnetic order. Next, we investigate the "clean" graphene quantum dots using Quantum Monte Carlo methods, which allow for inclusion of the correlations.

The work is organized as follows. In the first chapter, we review the properties of graphene, focusing on the electronic ones. In the second chapter, we describe the properties of graphene nanostructures, among which are the quantum dots that we investigate. The third chapter is a brief description of models of disorder, focusing on the one used in our calculation. Fourth chapter describes the methods used: SCF scheme for mean-field Hubbard model and the Quantum Monte Carlo methods. The last chapter describes the results we obtained.

Chapter 2

Graphene as a crystal

This chapter gives a review of properties of bulk graphene, focusing on the electronic ones, as well as some information on its fabrication and applications.

2.1 Introduction

Graphene is a two dimensional allotrope of carbon. One may think about graphene as a single layer of graphite: many graphene layers, connected by van der Waals forces, make up a graphite crystal. Because of that, graphene fragments may be created every time when one writes with a pencil, but it was not before 2004 that graphene was measured for the first time. Geim and Novoselov, who conducted these experiments, were awarded Nobel prize in 2010.

Since this discovery, it was found that graphene shows many extraordinary properties (for a good review see Nobel prize materials on graphene [1]).

The band structure of graphene is not usual. Graphene is a semimetal with no energy gap and linear low-energy dispersion (contrary to "ordinary" semiconductor where it is parabolic). This form of dispersion relation is responsible for an ambipolar field effect, in which there is either the electron or hole conductance. The measured value of electron mobility in graphene in room temperature is $15000 \text{ cm}^2\text{V}^{-1}\text{s}^{-1}$, which is remarkably high. Also, the linear band structure is the reason of unusual Landau level spectrum, proportional to $\pm\sqrt{N}$. This leads to the unusual quantum Hall effect, with Hall conductivities quantized to $\sigma_{xy} = \nu \frac{e^2}{h}$ with $\nu = \pm 4(n + \frac{1}{2}) = \pm 2, \pm 6, \pm 10, \dots$ (that is 4 times the unit of conductance due to spin and valley degeneracy). The inter-level spacing for lowest Landau levels is so high that it allows the observation of quantum Hall effect in room temperature.

Graphene's breaking strength is 42 N/m. This makes it about 100 times stronger than a layer of steel (of similar thickness). A 1 m^2 sheet of graphene can hold a weight of 4 kg. It means that

a hammock made of graphene can hold a cat, while, being one atom thick, it would weigh less than this cat's whisker.

The thermal conductivity of graphene is about $5000 \text{ Wm}^{-1}\text{K}^{-1}$, which is about 10 times larger than the thermal conductivity of copper. Graphene absorbs 2.3% of incident light intensity, so it is nearly transparent. This number is independent on the wavelength in the optical domain.

The electronic properties of graphene, connected with its strength, flexibility and atomic thickness, inspired the research into graphene electronics, which may one day replace the today's silicon technology [2]. The graphene field effect transistors [3], and even the first graphene-based integrated circuit (broadband radio frequency mixer), were created [4].

Transparency and good conductivity makes graphene a good candidate for transparent conductor to use for example in solar cells or touch screens [5]. For the latter, the researchers hope to employ the flexibility of graphene to create flexible screens. The first experimental solar cells were already created, although their performance was lower comparing to these used today. The fully functional touch screen using graphene was also already created [6]. Other possible applications in photonics or optoelectronic devices involve the organic light emitting diodes (OLED), ultrafast lasers or photodetectors [7]. Composites made using graphene are proposed to be used in lithium ion batteries, supercapacitors and fuel cells [8]. The 2D structure of graphene gives it highest possible surface-to-volume rate, which is very desirable when constructing gas sensor. Using graphene, it was possible for the first time to sense an absorption of a single molecule [9]. Among the application of graphene there is also a place for the less serious ones. During a study on permeation of gases through graphene oxide membranes, a first distillation of vodka using graphene was performed [10, 11]. Ted Kosmatka's spaceship is, although, still the pure fantasy.

Simultaneously to the development of graphene-based devices, much effort were done for finding better methods of creating graphene crystals. The first method, used by Geim and Novoselov [12, 13], was not suitable for mass production. A piece of highly-oriented pyrolytic graphite was repeatedly peeled off using the scotch tape, until a few layers thick pieces remained. These pieces were then pressed down on SiO_2 substrate. An interference technique, and atomic force microscopy, was used to check the thickness of these fragments and it appeared that some of them are indeed one-layer thick.

As an alternative method for creating graphene, chemical vapour deposition was proposed. Hydrocarbons, such as methane or acetylene, are deposited on substrates of for example Ni and Cu. Also, many other methods are investigated. One of them, for example, uses the sublimation of Si atoms from SiC, which result in graphitization of carbon on the surface. This method allows to form nanostructures by lithography technique. Another method consists of formation of graphite

oxide from graphite. It can be then chemically exfoliated. Then, in the single layers, the oxygen groups are reduced. A review of graphene creation methods can be found in [14].

2.2 Crystal structure

The lattice of graphene is honeycomb, with lattice constant $a = 1.42$ (see fig 2.1). Carbon possesses 4 valence electrons. The p_x, p_y (in-plane) and s orbitals hybridize into sp^2 , orbitals which form sigma bonds. These bonds are responsible for mechanical properties of graphene. Electronic properties are controlled by remaining p_z orbitals, which form out-of-plane π bonds.

An unit cell of graphene may be chosen as a rhombus, containing two atoms. The unit vectors can be defined as

$$\vec{a}_1 = \left[-\frac{a\sqrt{3}}{2}, \frac{3a}{2} \right], \quad \vec{a}_2 = \left[\frac{a\sqrt{3}}{2}, \frac{3a}{2} \right]. \quad (2.2.1)$$

The honeycomb lattice has a feature which will be crucial for many of the following consideration: bipartiteness. It can be divided into two sublattices, named A and B, originating from two atoms of the unit cell. Both of them are triangular. The definition of bipartite lattice is that if we connect all the pairs of nearest-neighbouring atoms, each atom of one sublattice connects only to the atoms of the other. This "sublattice symmetry" will have an important influence on electronic properties of graphene nanostructures.

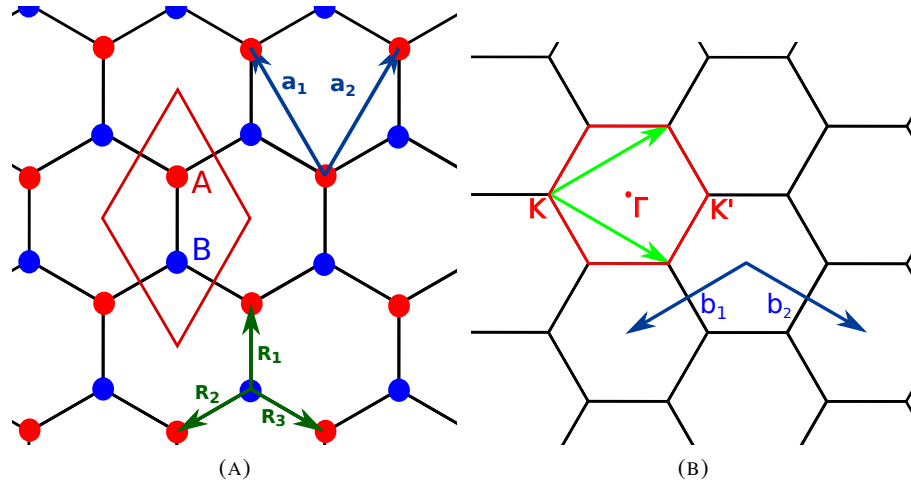


FIGURE 2.1: Honeycomb lattice of graphene. A) In real space: the unit cell (red), lattice vectors (blue) and nearest-neighbour vectors. B) In reciprocal space: the unit cell with characteristic points (red), the lattice vectors (blue), the equivalence of K points (green)

2.3 Electronic structure

2.3.1 Tight-binding model

As many theoretical results for graphene, its band structure was calculated long before its exfoliation. It was done in 1947 by Wallace [15], as a step in calculation of band structure of graphite.

Wallace used the tight-binding approximation, which is probably the simplest existing approximation for band structure - although it is sufficient to gather the basic quantitative and qualitative information about the electronic structure of the system, and will be used extensively in this thesis.

We start from a basis of atomic orbitals. The crucial idea of tight-binding approximation is that the matrix elements of crystal Hamiltonian are important only between close-lying orbitals. For now, we will use only the on-site (orbital with itself) and nearest-neighbour matrix elements, although later in this thesis we will also use the more distant ones.

As stated before, we will consider only the p_z orbitals. All the matrix elements between p_z orbitals and the rest are zero. Other orbitals also form energy bands, but it can be shown that for low energy properties (in which we are interested) the p_z block alone is sufficient.

Graphene is made of carbon atoms only, and all spacings between them are equal. That means all the matrix elements of the same kind (that is, all the on-site ones and all the nearest-neighbour ones) are equal. Moreover, the on-site element is diagonal. A multiplicity of a unit matrix can be always added to Hamiltonian to set the energy scale, so we can set the zero of energy so that the on-site element ϵ will vanish (the inequivalence between atoms, and the site-dependent on-site energy, which cannot be removed this way, will be introduced in chapter 3). Our Hamiltonian has therefore only one parameter, the nearest-neighbour matrix element t . We take it equal -2.84eV [16].

The periodicity puts constraints on the possible form of wave function, so we can use the basis of the Bloch sums,

$$\psi_T(\vec{k}, \vec{r}) = \frac{1}{\sqrt{N}} \sum_{\vec{R}_T} e^{i\vec{k} \cdot \vec{R}_T} \phi_T(\vec{r} - \vec{R}_T). \quad (2.3.1)$$

The Bloch sums are labelled by two indices: \vec{k} - a wave vector and $T = A, B$ - denoting the position of atom in the unit cell (see fig 2.1). Summation goes through all unit cells. Each of the carbon atoms in the unit cell (A and B) has its own Bloch sum. The Schrödinger equation can be written separately for each \vec{k} vector. Now, the problem is reduced to two-dimensional generalized eigenvalue equation.

We need only two types of matrix elements:

$$H_{AA}(\vec{k}) = H_{BB} = \frac{1}{N} \sum_{\vec{R}_{Ai}\vec{R}_{Aj}} e^{i\vec{k}(\vec{R}_{Aj}-\vec{R}_{Ai})} \langle \phi_A(\vec{R}-\vec{R}_{Ai}) | H | \phi_A(\vec{r}-\vec{R}_{Aj}) \rangle = \frac{1}{N} \sum_{\vec{R}_{Ai}} \varepsilon = \varepsilon = 0,$$

$$H_{AB}(\vec{k}) = H_{BA}^*(\vec{k}) = \frac{1}{N} \sum_{\vec{R}_{Ai}\vec{R}_{Bj}} e^{i\vec{k}(\vec{R}_{Bj}-\vec{R}_{Ai})} \langle \phi_A(\vec{R}-\vec{R}_{Ai}) | H | \phi_A(\vec{r}-\vec{R}_{Bj}) \rangle = \frac{1}{N} \sum_{\vec{R}_{Ai}} f(k)t = f(k)t, \quad (2.3.2)$$

where $f(\vec{k})$ is a sum of phase shifts related to nearest neighbours,

$$f(\vec{k}) = e^{i\vec{k}\cdot\vec{R}_1} + e^{i\vec{k}\cdot\vec{R}_2} + e^{i\vec{k}\cdot\vec{R}_3}, \quad (2.3.3)$$

where R_1, R_2, R_3 are vectors between nearest neighbours, originating at A atom (see fig 2.1). They are defined as

$$\vec{R}_1 = [0, a], \vec{R}_2 = \left[\frac{a\sqrt{3}}{2}, -\frac{a}{2} \right], \vec{R}_3 = \left[-\frac{a\sqrt{3}}{2}, -\frac{a}{2} \right]. \quad (2.3.4)$$

The Schrödinger equation can be written as a secular equation

$$H(k) \begin{bmatrix} A \\ B \end{bmatrix} = E(k) S(k) \begin{bmatrix} A \\ B \end{bmatrix}, \quad (2.3.5)$$

where A and B are the coefficients of the eigenfunction in the Bloch sum basis. S is a matrix of overlaps, arising from the non-orthogonality of the atomic p_z orbitals

$$S(k) = \begin{bmatrix} 1 & \int \psi_A^*(\vec{k}, \vec{r}) \psi_B(\vec{k}, \vec{r}) d\vec{r} \\ \int \psi_B^*(\vec{k}, \vec{r}) \psi_A(\vec{k}, \vec{r}) d\vec{r} & 1 \end{bmatrix}. \quad (2.3.6)$$

Due to strong localization of the atomic orbitals the overlap is small and can be neglected [17] (which mean treating the basis as orthogonal). The Schrödinger equation can be written as an eigenvalue equation

$$\begin{bmatrix} 0 & tf(k) \\ tf^*(k) & 0 \end{bmatrix} \begin{bmatrix} A \\ B \end{bmatrix} = E(k) \begin{bmatrix} A \\ B \end{bmatrix}. \quad (2.3.7)$$

The Hamiltonian is easy to diagonalize, and the resulting energy spectrum (Fig. 2.2) is

$$E(k) = \pm t|f(k)|. \quad (2.3.8)$$

The spectrum is symmetric with respect to Fermi level ($E=0$). We note that when overlap matrix elements are included, the spectrum is not symmetric anymore.

The eigenfunctions can be written as

$$\Psi_v(k) = \begin{bmatrix} 1 \\ \frac{f(k)}{|f(k)|} \end{bmatrix}, \Psi_c(k) = \begin{bmatrix} 1 \\ -\frac{f(k)}{|f(k)|} \end{bmatrix}, \quad (2.3.9)$$

where v and c refer to valence and conduction bands. The density of states of graphene in TB approximation can be also obtained analytically [18]; the plot is shown in fig 2.2. At the band crossing, DOS vanishes. Other characteristic feature are the two van Hove singularities at $\pm t$.

The most notable features of the energy spectrum are the absence of energy gap and the linear dispersion of energy near the Fermi level. The Brillouin zone of graphene is shown in Fig. 2.1 B). There are six points - six corners of the Brillouin zone - where the conduction and valence band touch. Only two of them, however, are not equivalent, that is, one cannot generate one by translation of the other by a reciprocal lattice vector (see Fig. 2.1). Let us denote them as K and K' . We note that $K' = -K$. The K vector may be found by searching for zeros of $f(k)$, and noting that $\vec{k} \cdot \vec{r}_i, i = 1, 2, 3$ must be the vertices of an equilateral triangle on the complex plane. One of the K points is

$$K = \left[\frac{4\pi\sqrt{3}}{9a}, 0 \right]. \quad (2.3.10)$$

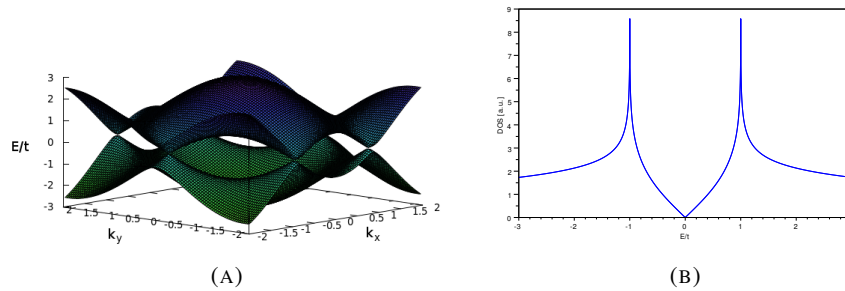


FIGURE 2.2: A) Graphene bandstructure, B) Graphene density of states

For the reasons that will be made clear below, these points are called Dirac points.

2.3.2 Dirac fermions

The low-energy properties of graphene can be derived by performing Taylor expansion of $f(\mathbf{x})$ in K or -K point [18–20]. Let us focus on K point, given by eq. 2.3.10,

$$\begin{aligned} f(\vec{K} + \vec{q}) &\approx f(\vec{K}) + \vec{q} \cdot \nabla f(\vec{k})|_{k=K} = i\vec{q} \cdot (r_1 e^{i\vec{K} \cdot \vec{r}_1} + r_2 e^{i\vec{K} \cdot \vec{r}_2} + r_3 e^{i\vec{K} \cdot \vec{r}_3}) = \\ &iq_y a + i\left(-\frac{1}{2} - \frac{\sqrt{3}}{2}\right)\left(-q_x \frac{\sqrt{3}}{2}a - q_y \frac{1}{2}\right) + i\left(-\frac{1}{2} + \frac{\sqrt{3}}{2}\right)\left(q_x \frac{\sqrt{3}}{2}a - q_y \frac{1}{2}\right) = \\ &\frac{3}{2}a(-q_x + iq_y). \end{aligned} \quad (2.3.11)$$

The resulting Hamiltonian is

$$H = \frac{3}{2}a \begin{bmatrix} 0 & -q_x + iq_y \\ -q_x - iq_y & 0 \end{bmatrix} = \frac{3}{2}at \vec{\sigma} \cdot \vec{q} \quad (2.3.12)$$

where $\vec{\sigma}$ is the vector of Pauli matrices: $[\sigma_x, \sigma_y]$ On the other hand, one can consider the Dirac hamiltonian:

$$H = \beta mc^2 + c\vec{\alpha} \cdot \vec{p} \quad (2.3.13)$$

In case of two dimensions, the α matrices are simply the Pauli matrices. So, if we put the mass equal to zero, the Hamiltonian starts to resemble the graphene one. That means that the low-energy excitations in graphene have the form of *massless Dirac fermions*. They behave like ultra-relativistic particles, with "speed of light" equal $\frac{3}{2}at$.

Now let us examine these connections closer. First, we note that the "real" Dirac fermions possess two- (or more-) component wavefunction (spinor). For graphene Dirac fermions, the role of spin is played by sublattices, with no connection to the real spin which they also possess.

Secondly, the Taylor expansion is carried *separately* for two "valleys": K and -K. Therefore, Dirac fermion bands are not two-fold (spin), but four (spin+valley) degenerate. It can be written explicitly using the four-component form of wavefunction.

One of the effect specific for relativistic particles, which is mimicked by graphene electrons, is the so-called Klein tunnelling. For particles with relativistic speeds, the probability of tunneling through a potential barrier becomes high, even reaching one. The occurrence of the similar effect in graphene leads to the conclusion that one cannot confine an electron in graphene in a "standard" way, by introducing external potential. This limits the applications of graphene, for example in electronics. In order to confine carriers, other methods should be used - e.g breaking the sublattice symmetry and then introducing the potential, or simply "cutting" graphene out of the infinite plane. In this work we will focus on the second approach.

Chapter 3

Graphene nanostructures

This chapter describes the properties of nanosize fragments of graphene. We describe the methods of fabrication of such structures. Then we describe their electronic and magnetic properties and the geometrical features on which they depend.

3.1 Experimental realization of graphene nanostructures

There are several methods proposed for creation of finite graphene structures (see Fig. 3.1). First, one may literally cut the graphene sheet into smaller ones [21, 22]. A Fe or Ni nanoparticle is placed on the graphene sheet, and serves as a catalyst for hydrogenation of carbon. The adhesion forces make the nanoparticle move along one crystallographic direction, which results in creation of straight trench in the graphene sheet. On the other hand, small graphene nanoflakes (graphene quantum dots) with well-defined edges may be created by assembling a large, branched aromatic molecule from some smaller precursor molecules, and then dehydrogenation [23]. This method results in highly-symmetric nanoflakes, for example hexagons. Similar method was proposed for creation of long graphene strips called "graphene nanoribbons".

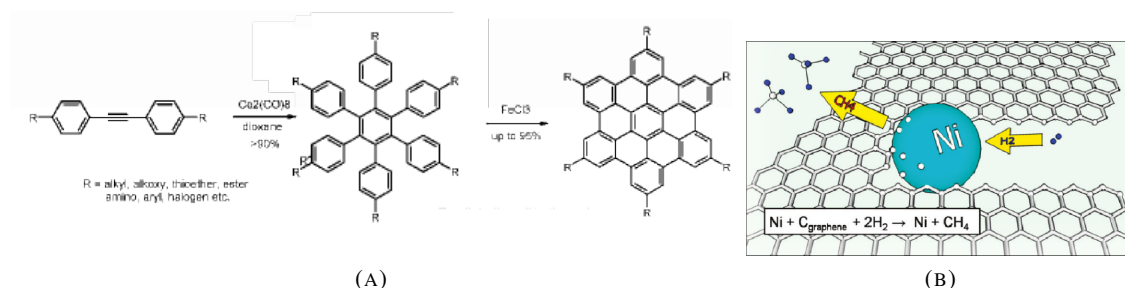


FIGURE 3.1: Two proposed methods for creation of graphene nanostructures: A) chemical assembly, B) chemical etching (reprinted from [22]) and [23].

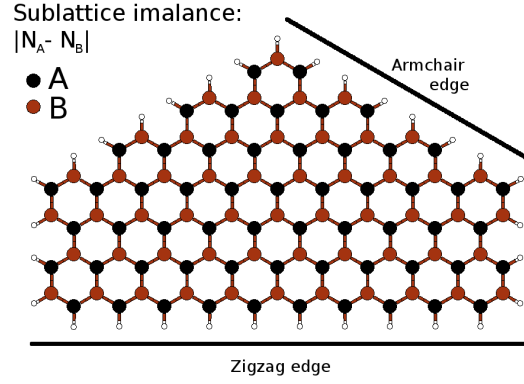


FIGURE 3.2: Basic geometrical concepts in graphene quantum dots: sublattice imbalance and two basic edge types. Black and brown atoms are carbon belonging to two different sublattices. The white atoms at the edges are hydrogen atoms.

3.2 Edges of graphene

The edge of graphene can be "cut" in any direction. However, there are two directions in which the edge is most stable. They are done along the basic crystallographic directions and were dubbed "zigzag" and "armchair" (see Fig. 3.2).

The termination of graphene sheet leaves one unsaturated bond per edge carbon atom. This means that either the hexagonal structure gets distorted at the edge, or other atoms (or groups) are attached to the edge atoms. In this work we assume that all the edges are "perfect", i.e. all the "dangling bonds" are saturated by hydrogen atoms. These hydrogen-passivated edges behave in the same way as lattice artificially terminated at the edge, because the hydrogen atoms do not have the p_z orbitals and within the tight-binding approximation the hopping integral to them is zero.

3.3 Edge and shape influence on electronic and magnetic properties

The subject of this work are graphene quantum dots (GQD). These are finite flakes of graphene, in which the electrons are confined in every dimension. The size of GQDs described in this thesis ranges from a few tens to a thousand carbon atoms. Such flakes can have different shapes, differing in the number and type (armchair or zigzag) of edges.

As examples, we choose three different GQDs: hexagon with armchair edges (1014 atoms), hexagon with zigzag edges (1014 atoms) and triangle (1021 atoms), also with zigzag edges. These shapes are commonly used examples, extensively investigated [24–30]. We use the tight-binding approximation. The basis consists of one p_z orbital per carbon atom. We assume all the edges are passivated by hydrogen. The matrix elements are: the nearest-neighbour term

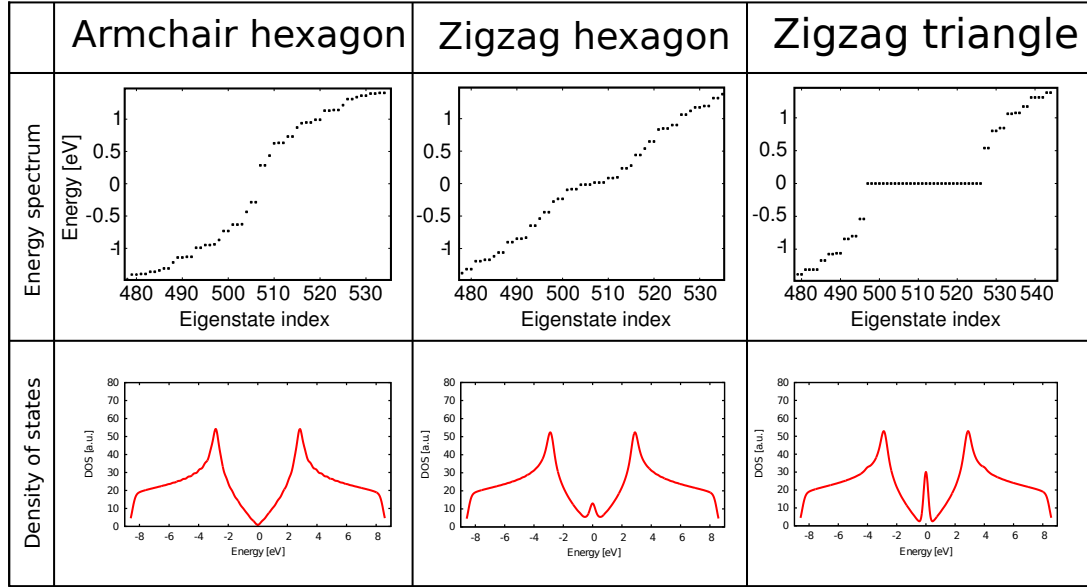


FIGURE 3.3: Comparison of tight-binding results for three graphene quantum dots of atom number around 1000

$t = -2.84\text{eV}$ and the second-nearest-neighbour term $t_2 = -0.1$. The Hamiltonian matrix is diagonalized numerically¹. In second quantization, the Hamiltonian may be written as

$$H_{TB} = t \sum_{\langle i,j \rangle} c_i^\dagger c_j + t_2 \sum_{\langle\langle i,j \rangle\rangle} c_i^\dagger c_j \quad (3.3.1)$$

where $\langle \rangle$ denotes the nearest neighbours, $\langle\langle \rangle\rangle$ denotes the second-nearest neighbours, and c_i^\dagger, c_i is, respectively, the creation and annihilation operator of p_z orbital at node i .

Fig. 3.3 shows the energy spectra of these structures, near the Fermi level (which is at zero energy). It can be seen that for two hexagons, the energy gap is lower for the zigzag one. In the case of zigzag triangle, the gap is similar to this of armchair hexagon, but there exist a 30-fold degenerate level in the middle of the gap. The degeneracy is exact in nearest-neighbour approximation, and it is slightly lifted when the next-nearest-neighbour hopping integrals are introduced.

Fig. 3.3 shows also the corresponding densities of states for the considered nanoflakes. These plots are created by convolution of discrete spectrum with gaussian kernel. They are similar to the density of states of bulk graphene, with the characteristic van Hove singularities - except from the vicinity of Fermi level. There, the DOS looks different for each structure. The armchair hexagon DOS still resembles the bulk one. In the case of zigzag hexagon a peak arises. Although an energy gap here exists, it is not visible because of overlap of the Gaussians. The peak is even higher in the case of the zigzag triangle.

¹Our diagonalization was done with Eigen C++ library.

To investigate the origin of this differences, let us take a closer look at the states near the Fermi level. The state just above the Fermi level for the zigzag hexagon is localized at the edges, as well as a few above and below (see Fig. 3.4 for corresponding state of a smaller zigzag hexagon). This is different for corresponding state of armchair hexagon, which has no such feature. The degenerate shell of zigzag triangle is also localized at the edges. Fig. 3.4 shows the sum of electronic densities of all the states in this shell (for a triangle composed of 33 atoms). Existence of the edge states is a general property of zigzag edges [31] and was confirmed experimentally[32]. On amchair edges no such states exist.

Now we know the difference between zigzag and armchair edges. But we have two structures, triangle and hexagon, with all-zigzag edges, and different density of states profiles. What is the difference between them?

The answer lies in the bipartiteness of the graphene lattice [33, 34]. Let us order the basis so that all the orbitals of A sublattice go first, and then go all the B sublattice orbitals. Because the Hamiltonian matrix elements (in nearest-neighbour approximation) are zero between orbitals of the same sublattice, the Hamiltonian in this basis is block-offdiagonal

$$H = \left[\begin{array}{c|c} 0 & T \\ \hline T^{\dagger \text{analogical}} & 0 \end{array} \right]. \quad (3.3.2)$$

The T and T^{\dagger} are the matrices composed of 0's and t 's. The T matrix has dimension $N_A \times N_B$. The rank of H (the number of linearly independent rows or columns is $2 \min\{N_A, N_B\}$). The nullity of H (number of zero-eigenvalue eigenvectors) can be calculated using rank-nullity theorem:

$$\text{rank } H + \text{nullity } H = N, \quad (3.3.3)$$

where $N = N_A + N_B$ is the size of the matrix. Then

$$\text{nullity } H = N - 2 \min\{N_A, N_B\} = |N_A - N_B|. \quad (3.3.4)$$

Therefore, the degeneracy of zero-energy level is equal to the difference of numbers of A and B atoms, which is called the *sublattice imbalance*. This quantity in our zigzag triangle is exactly 30. In zigzag hexagon, it is zero - thus, although the edge states exist, there are not exactly at the Fermi level and a finite gap between them exist. But the existence of the edge states make the gap lower than in armchair hexagon, which also has sublattice imbalance equal zero.

The degeneracy of zero-energy shell is perfect only in nearest-neighbour model, and it is slightly lifted when the second-nearest neighbour matrix elements are introduced.

The two geometrical features, the sublattice imbalance and the edge type, determine the low-energy spectrum of all graphene nanoflakes. The same features control the magnetic order in

these structures. Within the Hubbard model (which will be described in Chapter 5) there is a theorem by Lieb [35], which states that for the half-filled (one electron per node) even lattices, i.e. with even number of nodes, the ground state has the total spin of absolute value equal to

$$S_{tot} = \frac{|N_A - N_B|}{2} \quad (3.3.5)$$

That means that the zigzag triangle has nonzero total magnetic moment, while both hexagons have zero.

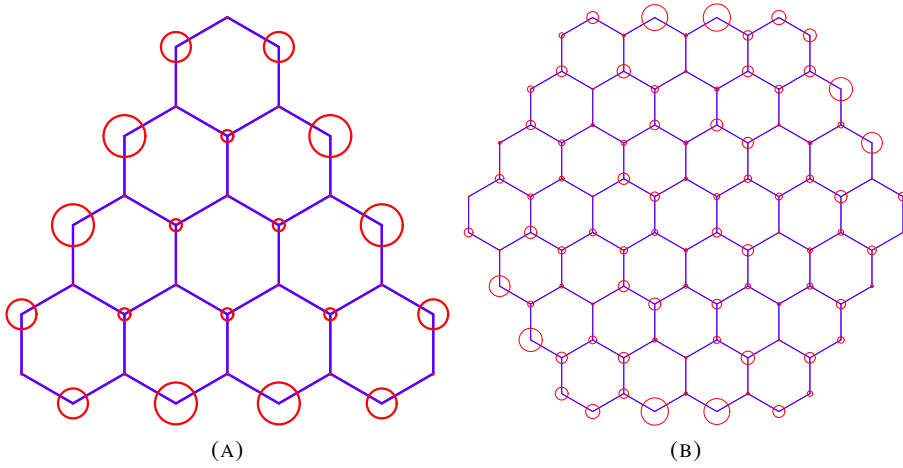


FIGURE 3.4: A) Edge states in zigzag triangle (sum of electronic density over the whole degenerate shell). B) One of the edge states in zigzag hexagon (just above the Fermi level).

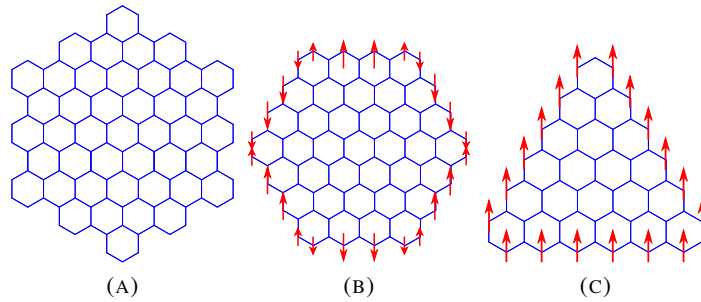


FIGURE 3.5: Schematic view of magnetic order in graphene nanostructures: A) unpolarized armchair hexagon, B) antiferromagnetic zigzag hexagon, C) ferromagnetic zigzag triangle.

The magnetism is arising from the states near the Fermi level, which, in case of the zigzag structures are the edge states. The spin density, defined as the density difference between spin up and spin down electrons $n_{i\uparrow} - n_{i\downarrow}$, in both of these structures is localized at the edges (see Fig. 3.5). In the zigzag triangle, the order is ferromagnetic - all the edges have the same sign of spin density. In zigzag hexagon, three edges are polarized with positive, and three with negative spin density, which makes the order antiferromagnetic. It is worth noting that the sublattices are polarized with opposite sign in both cases - yet the triangle has edges belonging to one

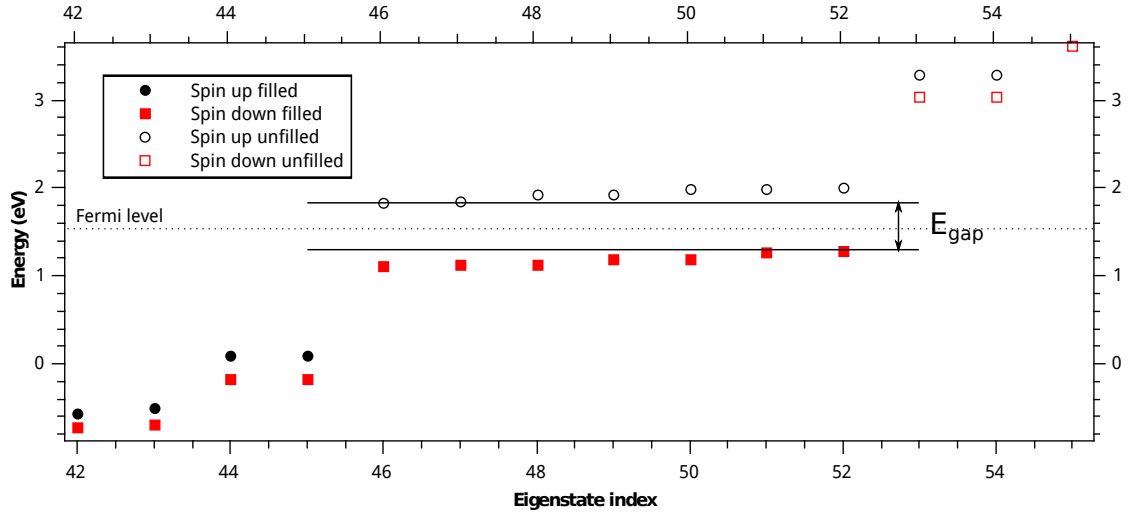


FIGURE 3.6: Hubbard spectrum for 97-atom zigzag triangle. The spin gap opens at the Fermi level.

sublattice, and hexagon to both. The armchair hexagon has no magnetic order because there is no edge states.

For structures with unbalanced lattice, for example for our zigzag triangle, a spin gap opens in the energy spectrum in the degenerate zero-energy shell (see Fig. 3.6).

The calculation within density functional theory confirmed that the Hubbard model is a good approximation of the electronic structures of charge-neutral (that is, half-filled) graphene nanoflakes, and consequently the Lieb theorem is valid [26]. For charged nanoflakes, the correlations between electrons can be strong enough to make this approximation invalid [30].

3.4 Nanoribbons

Similar considerations may be applied to narrow strips of graphene called *nanoribbons* [36, 37]. The difference is that now we have a crystal infinite in one dimension. But still there is a difference in edge effects; in the one electron approximation the armchair ribbons have gapped spectrum, while the zigzag ones have no gap and a nearly flat band at the Fermi level. The zigzag edges also get spin polarized and lead to the opening of an energy gap.

Chapter 4

Disorder in graphene

This chapter describes the types of disorder present in graphene and the models used to investigate them numerically or analytically. We want to introduce the Anderson disorder model, which was used in our calculation, but also to some information on other models and types of disorder, in order to give the reader the context of diversity of the subject. The chapter is based mostly on a few review articles [34, 38–40].

4.1 Sources of disorder

In the previous chapters, we considered systems with perfect (perfectly periodic, at least within the borders of a nanostructure) lattices, or at least implicitly we assumed that they are well described by approximation of perfect lattice. This, of course, is not always the case. There is a lot of reasons for which the structure can deviate from perfection. And there is a lot of ways in which this deviation can happen.

Some atoms in the lattice can be missing, creating vacancies. The bonds may deviate from hexagonal ordering, creating topological defects, e.g. Stone-Wales defects (pentagon-heptagon pairs). Some methods of fabrication of nanostructures results in rough edges, which are neither purely armchair nor zigzag. The disorder may also be brought by atoms of other elements: adsorbates and impurities. Also, graphene sheets are usually not perfectly flat. They have the tendency to stabilize themselves by forming ripples.

Another source of disorder comes into play for epitaxial graphene. The charge traps and charged impurities that are present in the substrate are the source of electrostatic potentials. Also, the graphene mimics the behaviour of substrate. When substrate changes height, the graphene sheet follows these changes.

4.2 Modelling disorder

There are different approaches to modelling disorder. For our considerations, we can divide them into three groups:

- "Accurate" models, when the exact chemical structure of the defect is investigated. These are e.g. DFT calculation of Stone-Wales defects, or adsorption of certain type of atoms.
- "Generic" models, which consist of adding to the Dirac Hamiltonian terms breaking specified symmetries. This approach, although it works good, gives no idea about the microscopic origin of these terms.
- "Simplified microscopic" approach. We can incorporate some simplified models of disorder into the tight-binding (or Dirac fermion) model. This allows to give general statements on the influence of disorder on the properties of graphene, taking into account their microscopic nature, but without going into chemical details (and losing the accuracy).

In this thesis we use a model that belongs to the third group. Because of that, here we present a bunch of models belonging to this group, including the one used by us.

Change of the bond lengths (e.g. due to conformation to substrate) will be reflected by the change of hopping integral. The variation of bond lengths may be random and independent for each bond. If, on the other hand, it is smooth in the atomic scale (in Fourier space, it does not generate a change in momentum that couples the two inequivalent Dirac cones), this changes may be approximated by vector and scalar potentials acting on the Dirac fermions. Strain in graphene can generate "pseudo-magnetic fields", which differ from the real magnetic field by the fact they do not break the time reversal symmetry - it is broken only inside each Dirac cone separately.

If the graphene surface is bent (e.g. forming ripples), then the vertical angles between orbitals change. The subspaces of p_z orbitals and the rest of the atomic orbitals are no longer orthogonal. This can be approximated by a scalar potential, acting on the Dirac fermions, proportional to the square of local curvature of the graphene sheet.

The on-site energy in the tight-binding model also can be varied. The simplest version, very often used (and the one used in this thesis), is the Anderson disorder, in which the on-site energy is random and independent at each lattice node. The energy is often taken from the "box distribution", i.e. the uniform distribution on the range $[-W/2, W/2]$, where W is a parameter describing disorder strength. This random variation may be applied everywhere, or just on the edges, reflecting the supposition that the edges may be more prone to disorder. The Anderson

disorder is somehow a basic and "generic" model of disorder, often used in works on disordered systems.

A similar model is the "binary alloy model", in which the on-site energy can take two selected values, with given probabilities. This model is used to simulate the effect of hydrogen adsorption on graphene [41].

On the other hand, one may think about models in which the on-site energy on one site is dependent on the on-site energies on the other ones. This is often used to model the impurities with long-range potentials. A given number of impurities is placed in random positions. Then, the on-site energies are taken as a sum of Gaussians centered at the impurities.

Instead of changing the parameters, one can also change the lattice structure. The vacancies are easily introduced into the tight-binding model by removing random sites. The roughness of edges, resulting from fabrication imperfection, may be modelled in similar way, by removing random atoms from the edges. Topological defects like pentagon-heptagon pairs can be also modelled in tight-binding approximation. Their approximation in Dirac fermion models are gauge fields which act on valley and sublattice indices.

4.3 Disorder and conductivity

Although this work does not cover the problem of transport by any means, it may be instructive to look at the effect of disorder on conductivity in graphene, to see how different the action of disorder may be depending on its form. One usually starts from semi-classical result for conductivity and look for the quantum corrections, due to quantum interference effects resulting from multiple scattering on various types of impurities.

Considering the disorder described by on-site energy variation, we can divide it into two categories: the short- and long-range disorder. The former varies on scale short enough to allow scattering between two Dirac cones, while the latter does not. The Anderson and binary alloy disorder models belong to the first class, while Gaussian impurities belong to the second.

The short-range disorder is responsible for conductivity-lowering correction known as weak localization. Long-range disorder does exactly the opposite - it increases the conductivity in the so-called weak antilocalization. Both of these corrections may be suppressed by ripples. The action of pseudo-magnetic fields is similar to the true one; it gives an additional phase factor, which destroys the interference effects.

4.4 Anderson disorder in graphene nanostructures

In the following work, we will focus only on the Anderson disorder model. This kind of disorder (along other short-range types of disorder) can lead to so-called Anderson localization [42, 43] - a transition from extended states, which spread through the whole structure, to the localized ones, which are confined in a smaller region. This can be also viewed from the point of view of time evolution: if a localized state (not an eigenstate) is created, it diffuses and spreads, but when the Anderson localization is taking place, this diffusion is suppressed and the state remains localized.

The subject whether this process really takes place in the infinite graphene is a difficult question, and, to my current knowledge, it is not solved. But, certainly, the numerical simulation show the localization takes place in the graphene nanoribbons.

An example of a transition from extended to localized eigenstates in a zigzag nanoribbon (numerical results by Schubert et al [44]) is shown in Fig. 4.1 Similar behaviour is seen if the disorder is limited only to edges, although then it is present only in the vicinity of the edges.

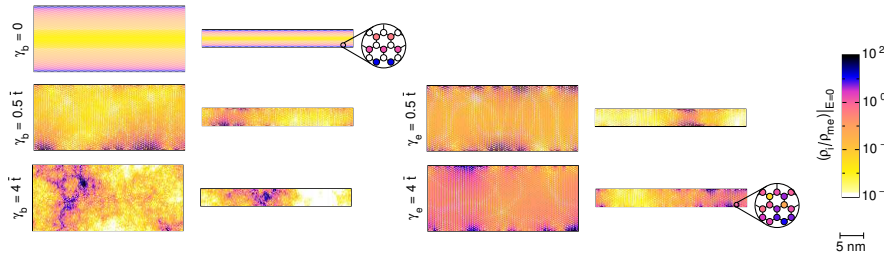


FIGURE 4.1: Numerically calculated local density of states at Fermi level for zigzag nanoribbons (adapted from [44].)

The influence of the bulk and edge Anderson disorder on the density of states of zigzag and armchair graphene nanoribbons (results by Schubert et al. [44] and Nemec et al. [45]) is shown in the Fig. 4.2. These results are the average DOS. Although the real system would have one particular configuration of disorder, the averaging allows to capture some general properties of disorder influence. Also, an experiment in which a large ensemble of nanostructures is investigated would give the averaged results. The disorder smoothens the average DOS, although edge disorder acts considerably weaker than the bulk one. The results for smaller bulk disorder shows which regions are most affected by it: the peaks in density of states at van Hove singularities or coming from edge states. The comparison of edge and bulk disorder in armchair nanoribbons shows that the results are similar when the sum of standard deviations over all atoms is the same. However, one may expect that this rule may be broken in zigzag ribbons, where the edge states would appear.

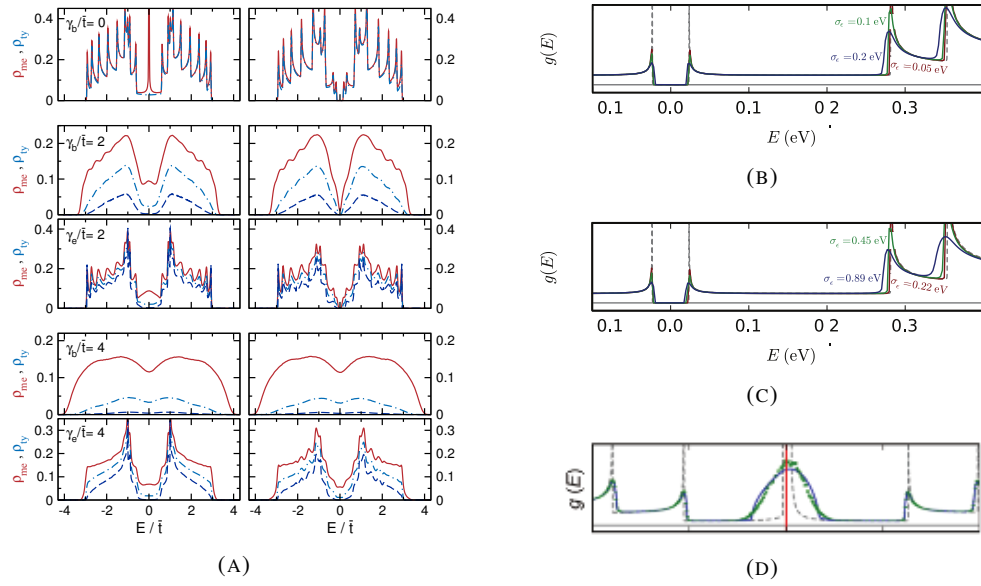


FIGURE 4.2: Density of states of disordered nanoribbons. A) Results of numerical simulation by Schubert [44]. The "average DOS" (red) is the local density of states averaged by position and disorder configurations, so it corresponds to our average DOS. B)-D) Analytical and numerical results by Nemec [45] B) Armchair ribbon, bulk disorder. C) Armchair ribbon, edge disorder (with sum of standard deviations on all lattice nodes corresponding to these from bulk disorder). D) Zigzag ribbon, bulk disorder.

The effect of disorder on density of states of graphene quantum dots was studied by Pal et al. [46]. He found out that the smoothing of DOS happens for bulk disorder, but not for the edge one (see Fig. 4.3). The dots investigated by Pal are, however, different than these described in previous chapters, they are formed using staggered sublattice potential to open energy gap and electrostatic potential to confine the electrons. There exist a number of works on Anderson disorder in "our" type of graphene quantum dots, but they usually concentrate on the transport properties and statistics of energy levels, which are beyond the scope of the thesis [47–49].

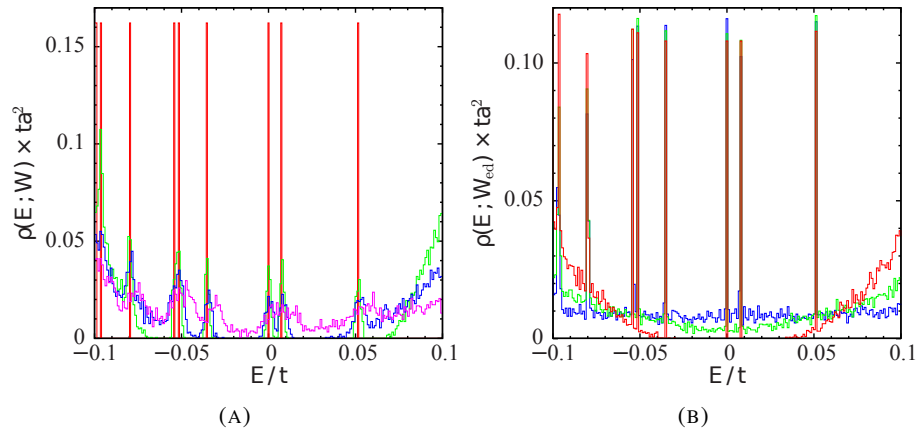


FIGURE 4.3: Numerically calculated density of states for disordered electrostatically-induced graphene quantum dots (adapted from [46]). A) Bulk disorder. B) Edge disorder.

Chapter 5

Methodology

In this chapter, we describe the methods that we will use in our calculations. One of them, the tight binding model, was described in Chapter 1. This model, although, does not include the electron-electron interaction. Therefore it neglects all the magnetic effects. Below we describe its simple extension to simple interacting model, the Hubbard model, and its mean-field approximation. Also, we describe the quantum Monte Carlo methods, that allow for inclusion of electronic correlation, although they are much more computationally demanding. The effects of disorder are investigated by the Hubbard model only, while the non-disordered systems are also studied with QMC.

5.1 The many-electron Hamiltonian

The general Hamiltonian, containing one-particle and two-particle operators (without spin-flipping) can be written as

$$H = \sum_{i,j,\sigma} \langle i|h|j \rangle c_i^\dagger c_j + \frac{1}{2} \sum_{i,j,k,l,\sigma_1,\sigma_2} \langle i\sigma_1, j\sigma_2|g|\sigma_2k, l\sigma_1 \rangle c_{i,\sigma_1}^\dagger c_{j,\sigma_2}^\dagger c_{k,\sigma_2} c_{l,\sigma_1}, \quad (5.1.1)$$

where $c_{i,\sigma}$ and $c_{i,\sigma}^\dagger$ is, respectively, the creation and annihilation operator of p_z orbital at node i and with spin σ . Operator h is the one-electron part of the Hamiltonian (for example, in tight-binding model $\langle i|h|j \rangle$ is equal t for nearest neighbours, t_2 or 0 for next-nearest neighbours and zero otherwise), while g is the operator describing electron-electron interaction. For Coulomb interaction, we have

$$\langle i\sigma_1 j\sigma_2|h|k\sigma_2 l\sigma_1 \rangle = \int d\vec{r}_1 \int d\vec{r}_2 \frac{\phi_{i\sigma_1}^*(\vec{r}_1) \phi_{j\sigma_2}^*(\vec{r}_2) \phi_{k\sigma_2}(\vec{r}_2) \phi_{l\sigma_1}(\vec{r}_1)}{\epsilon |\vec{r}_2 - \vec{r}_1|}, \quad (5.1.2)$$

where $\phi_{i\sigma}$ is the atomic orbital p_z at node i and with spin s .

5.1.1 Hubbard model

The Coulomb interaction strength vanishes quickly with the distance. We can make an approximation in which the interaction matrix element is nonzero only when two electrons are at the same atomic orbital. This approximation, along with approximation of the one-electron part with tight-binding Hamiltonian, defines the Hubbard model

$$H_{Hubb} = H_{TB} + \frac{1}{2}U \sum_{i\sigma_1\sigma_2} c_{i,\sigma_1}^\dagger c_{i,\sigma_2}^\dagger c_{i,\sigma_2} c_{i,\sigma_1}, \quad (5.1.3)$$

where U is the on-site interaction matrix element. If $\sigma_1 = \sigma_2$, then there is a double action of the same creation operator, so the result is zero. Using this remark, we can write the Hubbard Hamiltonian as

$$H_{Hubb} = H_{TB} + U \sum_i n_{i,\uparrow} n_{i,\downarrow} \quad (5.1.4)$$

where $n_{i,\sigma} = c_{i\sigma}^\dagger c_{i\sigma}$ is a number operator of electrons on node i and with spin σ .

5.2 Mean-field procedure for Hubbard model

Diagonalizing the Hubbard Hamiltonian exactly is computationally impossible even for relatively small systems due to large Hilbert spaces of many-body functions. Therefore we use the mean-field approximation. We assume that the deviation of electron density from the average is small, and we can approximate the many-electron problem by one-electron problem in averaged field coming from other electrons.

We introduce the operators of deviation from average:

$$d_{i,\sigma} = n_{i,\sigma} - \langle n_{i,\sigma} \rangle. \quad (5.2.1)$$

The Hubbard Hamiltonian can be now written as

$$\begin{aligned} H_{Hubb} &= H_{TB} + U \sum_i (d_{i,\uparrow} + \langle n_{i,\uparrow} \rangle)(d_{i,\downarrow} + \langle n_{i,\downarrow} \rangle) = \\ &= H_{TB} + U \sum_i (d_{i,\uparrow} d_{i,\downarrow} + d_{i,\uparrow} \langle n_{i,\downarrow} \rangle + d_{i,\downarrow} \langle n_{i,\uparrow} \rangle + \langle n_{i,\uparrow} \rangle \langle n_{i,\downarrow} \rangle). \end{aligned} \quad (5.2.2)$$

The essence of mean-field approximation is the assumption that the first, quadratic term in the sum may be neglected. Now, the Hamiltonian contains only one-electron operators.

$$H_{MF} = H_{TB} + U \sum_i (n_{i,\uparrow} \langle n_{i,\downarrow} \rangle + n_{i,\downarrow} \langle n_{i,\uparrow} \rangle - \langle n_{i,\uparrow} \rangle \langle n_{i,\downarrow} \rangle). \quad (5.2.3)$$

The last term in the sum gives a constant, so it may be compensated by a shift in the energy scale, and so, it is usually neglected.

How to calculate the averages? We must specify the form of many-electron wave functions. Within the mean-field approximation we assume that the wave function is a single Slater determinant of the one-electron eigenstates of one-particle Hamiltonian from Eq. 5.2.3. Then the Slater determinant is also an eigenfunction of this Hamiltonian. We construct the Slater determinant by filling N_\uparrow spin up and N_\downarrow spin down lowest energy single-particle eigenstates

$$|\psi\rangle = \prod_{p=1}^{N_\uparrow} a_{p\uparrow}^\dagger \prod_{p=1}^{N_\downarrow} a_{p\downarrow}^\dagger |0\rangle. \quad (5.2.4)$$

We denote the creation annihilation operators of one-particle eigenstates by a^\dagger and a , to distinguish them from the atomic orbital operators c^\dagger and c . Also, we reserve indices p, q, r, s for the one-particle wave functions, while i, j, k, l will refer to atomic orbitals. The single-particle eigenstate creation and annihilation operators can be written in the atomic orbital basis

$$a_{p\sigma} = \sum_j A_{pj\sigma} c_{j\sigma}, \quad a_{p\sigma}^\dagger = \sum_j A_{pj\sigma}^* c_{j\sigma}^\dagger, \quad (5.2.5)$$

where $A_{pj\sigma}$ are the coefficients of expansion (the eigenstates may be different for different spin therefore the spin index is included). Using this expansion, the average electron number is

$$\langle n_{i,\sigma} \rangle = \sum_{p=1}^{N_\sigma} |A_{ip\sigma}|^2. \quad (5.2.6)$$

But still, we cannot compute it because we do not have the single-particle eigenvectors, and we cannot compute them, because we first need the averages to write the Hamiltonian. This eigenproblem needs to be solved self-consistently. We start from the pure tight-binding model. We diagonalize the Hamiltonian and use the resulting eigenvectors for the construction of next Hamiltonian. This is repeated, until the total energy of the system, i.e. the expectation value of energy in given many-particle state, converges.

Now, we will derive the expression for total energy. Because our Hamiltonian has only one-electron terms, we begin with discussing the expectation value of the form

$$\langle \psi | a_{p,\sigma}^\dagger a_{q,\sigma} | \psi \rangle. \quad (5.2.7)$$

Let us look closer at the action of an annihilation operator on $|\psi\rangle$

$$a_{p,\sigma} |\psi\rangle = a_{p,\sigma} \prod_{q=1}^{N_\uparrow} a_{q\uparrow}^\dagger \prod_{q=1}^{N_\downarrow} a_{q\downarrow}^\dagger |0\rangle. \quad (5.2.8)$$

If p is larger than N_σ , the $a_{p,\sigma}$ can be moved to the right (with only a change of sign), because it commutes with all the creation operators. Then, by acting an annihilation operator on $|0\rangle$ one gets zero. Therefore, the average from eq. 5.2.7 is nonzero only when the averaged creation and annihilation operators correspond to filled states. Let us assume for a moment that the creation operator under consideration has spin up, and $p < N_\uparrow$. Then

$$\begin{aligned} a_{p\uparrow} a_{1,\uparrow}^\dagger \dots a_{N_\uparrow,\uparrow}^\dagger a_{1,\downarrow}^\dagger \dots a_{N_\downarrow,\downarrow}^\dagger |0\rangle &= (-1)^{p-1} a_{1,\uparrow}^\dagger \dots a_{p,\uparrow} a_{p,\uparrow}^\dagger \dots a_{N_\uparrow,\uparrow}^\dagger a_{1,\downarrow}^\dagger \dots a_{N_\downarrow,\downarrow}^\dagger |0\rangle = \\ &= (-1)^{p-1} a_{1,\uparrow}^\dagger \dots (1 - a_{p,\uparrow}^\dagger a_{p,\uparrow}) \dots a_{N_\uparrow,\uparrow}^\dagger a_{1,\downarrow}^\dagger \dots a_{N_\downarrow,\downarrow}^\dagger |0\rangle = \\ &= (-1)^{p-1} a_{1,\uparrow}^\dagger \dots a_{p-1,\uparrow} a_{p+1,\uparrow} \dots a_{N_\uparrow,\uparrow}^\dagger a_{1,\downarrow}^\dagger \dots a_{N_\downarrow,\downarrow}^\dagger |0\rangle + (-1)^{p-1} a_{1,\uparrow}^\dagger \dots a_{p,\uparrow} a_{p,\uparrow}^\dagger \dots a_{N_\uparrow,\uparrow}^\dagger a_{1,\downarrow}^\dagger \dots a_{N_\downarrow,\downarrow}^\dagger |0\rangle = \\ &= (-1)^{p-1} |\psi'\rangle \quad (5.2.9) \end{aligned}$$

The last equality can be derived by moving annihilation operator in the second part to the right and acting on the ground state, which gives zero. The vector $|\psi'\rangle$ denotes a Slater determinant consisting of all the occupied spin-orbitals except $p\uparrow$. The -1 power in the case of spin down is $p-1+N_\uparrow$.

If we define $|\psi_1\rangle$ as a Slater determinant of all spin-orbitals except $p\sigma_1$ and $|\psi_2\rangle$ as the same Slater determinant but without $q\sigma_2$ then, according to the orthogonality rules in Fock space, we have

$$\langle \psi_1 | \psi_2 \rangle = \delta_{p,q} \delta_{\sigma_1 \sigma_2}. \quad (5.2.10)$$

Therefore, the expectation value in Eq. 5.2.7 is equal to

$$\langle \psi | a_{p,\sigma}^\dagger a_{q,\sigma} | \psi \rangle = \delta_{p,q}. \quad (5.2.11)$$

The expectation value of energy has the form

$$\langle E \rangle = \sum_{p,q,\sigma} \langle p\sigma | H_{MF} | q\sigma \rangle \langle \psi | a_{p\sigma}^\dagger a_{q\sigma} | \psi \rangle = \sum_p \langle p\sigma | H_{MF} | p\sigma \rangle, \quad (5.2.12)$$

where in the last equality we used eq. 5.2.11. To proceed, we have to write the matrix element in the atomic orbital basis. Then

$$\langle E \rangle = \sum_{p,i,j,\sigma} \langle p\sigma | i\sigma \rangle \langle i\sigma | H_{MF} | j\sigma \rangle \langle j\sigma | p\sigma \rangle = \sum_{p,i,j,\sigma} \langle i\sigma | H_{MF} | j\sigma \rangle A_{pi\sigma} A_{pj\sigma}^* \quad (5.2.13)$$

We know that

$$\langle i\sigma | H_{MF} | j\sigma \rangle = \begin{cases} t & \text{if } i, j \text{ are nearest neighbours,} \\ t_2 & \text{if } i, j \text{ are second nearest neighbours,} \\ \langle n_{i,\uparrow} \rangle & \text{if } i = j \text{ and } \sigma = \downarrow, \\ \langle n_{i,\downarrow} \rangle & \text{if } i = j \text{ and } \sigma = \uparrow. \end{cases} \quad (5.2.14)$$

Using these matrix element along with eq 5.2.6, we can write

$$\langle E \rangle = \sum_{p\sigma} \left(t \sum_{\langle i,j \rangle} A_{pi\sigma} A_{pj\sigma}^* + t_2 \sum_{\langle\langle i,j \rangle\rangle} A_{pi\sigma} A_{pj\sigma}^* \right) + 2U \sum_i \langle n_{i\uparrow} \rangle \langle n_{i\downarrow} \rangle. \quad (5.2.15)$$

Introducing again the neglected constant term from eq. 5.2.3, we can write

$$E_{tot} = \sum_{p\sigma} \left(t \sum_{\langle i,j \rangle} A_{pi\sigma} A_{pj\sigma}^* + t_2 \sum_{\langle\langle i,j \rangle\rangle} A_{pi\sigma} A_{pj\sigma}^* \right) + U \sum_i \langle n_{i\uparrow} \rangle \langle n_{i\downarrow} \rangle. \quad (5.2.16)$$

Now, let us summarize the procedure of calculation of the ground state of the mean-field Hubbard Hamiltonian.

1. Choose numbers of spin up and spin down electrons.
2. Solve the tight-binding eigenproblem.
3. Compute the averages. Using them, form two separate Hamiltonians (for spin up and spin down - our Hamiltonian is a block matrix). Solve them for eigenvalues and eigenstates.
4. Calculate the total energy.
5. Repeat steps 3 and 4 until the difference between total energies in two consecutive steps is less than desired.
6. Repeat steps 1-5 for different numbers of spin up and spin down electrons.
7. Compare the final total energies for all N_\uparrow and N_\downarrow . Choose the one with the lowest energy - it gives the ground state.

5.3 Quantum Monte Carlo

The mean field procedure does not include the correlations. The full many electron calculation, on the other hand, requires huge amount of computational power. A compromise between accuracy and computational cost can be reached within quantum Monte Carlo methods (QMC).

The name "Quantum Monte Carlo" includes many different methods that have in common only the fact that they use random sampling and are used for quantum systems. In this work, we will use two of them: Variational and Diffusion quantum Monte Carlo [50–54].

5.3.1 Variational Monte Carlo

5.3.1.1 Idea of the method

The Variational Monte Carlo is the simplest (conceptually) quantum Monte Carlo method. The idea is to employ the Monte Carlo integration technique in the variational scheme.

The variational theorem states that the expectation value of energy:

$$E = \frac{\langle \psi | H | \psi \rangle}{\langle \psi | \psi \rangle} = \frac{\int \psi^*(\vec{r}) H \psi(\vec{r}) d\vec{r}}{\int \psi^*(\vec{r}) \psi(\vec{r}) d\vec{r}}, \quad (5.3.1)$$

has global minimum at the ground state. Function ψ is the many-particle wave function and \vec{r} is the vector of positions of all electrons. Minimizing it is one way of searching for the true ground state of many-body Hamiltonian. Alternatively one may look for a minimum of variance

$$\sigma^2 = \frac{\int \psi^*(\vec{r}) H^2 \psi(\vec{r}) d\vec{r}}{\int \psi^*(\vec{r}) \psi(\vec{r}) d\vec{r}} - \left(\frac{\int \psi^*(\vec{r}) H \psi(\vec{r}) d\vec{r}}{\int \psi^*(\vec{r}) \psi(\vec{r}) d\vec{r}} \right)^2, \quad (5.3.2)$$

which is zero for exact eigenstates. Another option is to minimize the so-called median absolute deviation (MAD), which will be introduced in Section 2.3.1.4.

The idea of variational methods is to specify a form of the wave function dependent on a set of parameters, which are going to be optimized by searching for minimum of energy (or variance, or MAD).

5.3.1.2 Monte Carlo integration

The Monte Carlo scheme is used to calculate the integrals in 5.3.1 and 5.3.2. The basic version of Monte Carlo integration uses simple sampling. Let I denote the integral of function f in finite domain Ω

$$I = \int_{\Omega} f(\vec{x}) d\vec{x}. \quad (5.3.3)$$

The value of this integral may be approximated by

$$I \approx \frac{V}{N} \sum_{i=1}^N f(\vec{x}_i), \quad (5.3.4)$$

where the \vec{x}_i are points chosen from Ω with uniform distribution, and V is the volume of the Ω . This method is useful for approximation of many-dimensional integrals, for which the Newton-Cotes integration, which uses equally spaced points, is much less effective. However, if f has very high values in some regions of the domain, and small everywhere else, this method is ineffective, because many of the randomly selected points give a little contribution to the calculated value. Therefore, if one knows, at least approximately, where the high values lie, one may consider altering the \vec{x}_i distribution so that most of the points lie in the high-value region. If this distribution is $\rho(\vec{x}_i)$, then we can write the integral as:

$$I = \int \rho(\vec{x}) \frac{f(\vec{x})}{\rho(\vec{x})} d\vec{x}. \quad (5.3.5)$$

The weight $\rho(x)$ may be incorporated by selection of points with distribution $\rho(x)$. Then the integral may be approximated by

$$I \approx \frac{1}{N} \sum_{i=1}^N \frac{f(\vec{x}_i)}{\rho(\vec{x}_i)}. \quad (5.3.6)$$

Now, because of flatness of $f(x)/\rho(x)$, all the points give similar contributions to the result.

Let us now turn back to Eq. 5.3.1. We define the "local energy" as

$$E_L(\vec{r}) = \frac{H\psi(\vec{r})}{\psi(\vec{r})}, \quad (5.3.7)$$

If ψ is a true eigenstate of the Hamiltonian, then E_L is simply the energy eigenvalue (because $\frac{H\psi}{\psi} = \frac{E\psi}{\psi} = E$), so it is position independent. So we expect that, at least when ψ is close to the eigenstate, E_L is reasonably flat, and we want to choose it as a function we will sample in an importance sampling procedure. Now, we have to find the probability distribution from which we want to sample.

Using Eq. 5.3.7, we can write Eq. 5.3.1 as:

$$\langle E \rangle = \int \frac{|\psi(\vec{r})|^2 E_L(\vec{r})}{\int |\psi(\vec{r}')|^2 d\vec{r}'} d\vec{r} \quad (5.3.8)$$

This is a weighted average of E_L , with weight $\rho(\vec{r}) = \frac{|\psi(\vec{r})|^2}{\int |\psi(\vec{r}')|^2 d\vec{r}'}$. As described above, when calculating this integral with Monte Carlo scheme, we can select randomly \vec{r}_i 's with this probability.

5.3.1.3 Metropolis algorithm

The expression for $\rho(\vec{r})$ depends on chosen form of trial wave function and does not have to be any of the "common" probability distribution. Therefore, we will use the general method

for generating random variables of given distribution, the Metropolis algorithm. The idea is to construct a Markov chain, whose stationary distribution will be our desired distribution.

The algorithm will be as follows.

1. Choose some starting coordinates \vec{r} - a "starting position" of a random walker.
2. Choose the new, "trial" coordinates $\vec{r}_T = \vec{r} + \vec{\delta}$, where $\vec{\delta}$ is chosen from some distribution, eg. normal distribution.
3. Calculate the ratio $p = \rho(\vec{r}_T)/\rho(r) = [\psi(\vec{r}_T)/\psi(\vec{r})]^2$.
4. If $p > 1$, accept the "trial move" - put $\vec{r} = \vec{r}_T$.
If $p > 1$, accept the "trial move" with probability p - generate a random number and accept the move if it is less than p . If it is more then p , leave \vec{r} unchanged
5. Repeat steps 2-4 until the stationary distribution is reached (so-called *equilibration steps*).
6. Repeat steps 2-4, and take the values every n_{corr} steps as the desired random number.
The \vec{x} generated in consecutive steps are correlated, n_{corr} should be chosen larger than the correlation "time".

A "rule of thumb" is that, to get reasonable efficiency, the "acceptance ratio" (the ratio of steps when "trial move" is accepted to the number of all steps) should be about 0.5, the distribution according to which the "trial move" is chosen should be selected to meet this criterion. Usually, some parameters of this distribution are optimized during the "equilibration steps" to get the proper acceptance ratio).

5.3.1.4 Variance and MAD minimization using local energy

The same procedure may be used within the variance or MAD minimization approach. Using local energy, the variance (Eq. 5.3.2) may be written as

$$\sigma^2 = \frac{\int |\psi(\vec{r})|^2 |E_L(\vec{r}) - \langle E \rangle|^2 d\vec{r}}{\int |\psi(\vec{r})|^2 d\vec{r}}. \quad (5.3.9)$$

The median absolute deviation may be defined as

$$\text{MAD} = \frac{1}{N_c} \sum_{\vec{r}} |E_L(\vec{r}) - E_{median}|, \quad (5.3.10)$$

where the sum is over the random sampling points generated with the Monte Carlo procedure, N_c is the number of these points, and E_{median} is the median of local energy.

5.3.1.5 The form of the wave function

The commonly used form of many-body trial wave function can be written as:

$$\psi_{\vec{r}} = e^{J(\vec{r})} \sum_n c_n D_{n\uparrow} D_{n\downarrow}, \quad (5.3.11)$$

where $D_{n\uparrow}$ and $D_{n\downarrow}$ are the Slater determinants of single-particle molecular orbitals of spin up and spin down, respectively. In general, one can use a linear combination of several determinants, but often only one is used - and this will be the case in our calculation. Function J is the so-called Jastrow factor, which describes the correlation between electrons. In our calculation, it will have the form

$$J(\vec{r}) = \sum_{i=1}^{N-1} \sum_{j=i+1}^N u(r_{ij}) + \sum_{I=1}^{N_{ion}} \sum_{i=1}^N \chi_I(r_{iI}) + \sum_{I=1}^{N_{ion}} \sum_{i=1}^{N-1} \sum_{j=i+1}^N f_I(r_{iI}, r_{jI}, r_{ij}), \quad (5.3.12)$$

where $r_{i,j}$ is the distance between two electrons or electron and a ion (ion index is the capital I), u is the electron-electron term, χ is the electron-nucleus term, while f is the three-body term dependent on position of two electrons and a nucleus. The functions involving nuclei are different for different chemical elements in the system. All three functions can in general be spin-dependent.

The u , χ and f functions are approximated by their first terms of the Taylor expansion, and coefficients of these expansions are the optimization parameters of our wave function. Also, they are forced to go to zero at the cutoff length, which may be also an optimizable parameters (the functions are also forced to have two or three continuous derivatives there). The Slater determinant part is usually not optimized and is taken from other calculations, using e.g. the Hartree-Fock or DFT methods.

5.3.1.6 Cusp conditions

The parameters of Jastrow factor are not independent. They should satisfy the so-called cusp conditions [55]. The reason is that the Coulomb potential, which describes the electron-electron and electron-nucleus interaction, diverges as the distance between the particles goes to zero. Imposing a certain form of wave function can cancel this divergence, if it is chosen so that the kinetic energy also diverges, but with opposite sign.

We want the energy to be finite

$$H\psi = -\sum_i \frac{\nabla_i^2 \psi}{2m_i} + \sum_{i,j} \frac{q_i q_j}{r_{ij}} + \sum_{i,I} \frac{q_i q_I}{r_{iI}} \psi < \infty \quad (5.3.13)$$

where we use atomic units, so $\hbar = \frac{1}{4\pi\epsilon_0} = 1$. We pick two electrons and assume that all the other electrons and ions are distant, so we can neglect their contributions. Then we can use the center of mass coordinates:

$$-\frac{\nabla_r^2 \psi}{2\mu\psi} - \frac{\nabla_R^2 \psi}{2(m_1 + m_2)} + \frac{q_1 q_2}{r} \psi < \infty, \quad (5.3.14)$$

where $R = \frac{r_1 m_1 + r_2 m_2}{m_1 + m_2}$, $r = r_1 - r_2$ and $\frac{1}{\mu} = \frac{1}{m_1} + \frac{1}{m_2}$. Because we have two electrons, then $R = \frac{r_1 + r_2}{2}$ and $\mu = m/2$

We do not care about the center-of-mass kinetic part, we assume that it already is finite, so let us omit it. Then, we can rewrite the equation in the spherical coordinates, centered at the center of mass of two electrons. The spherical Laplacian is

$$\nabla^2 = \frac{1}{r^2} \frac{\partial}{\partial r} \left(r^2 \frac{\partial}{\partial r} \right) + \frac{1}{r^2 \sin^2 \phi} \frac{\partial^2}{\partial \theta^2} + \frac{1}{r^2 \sin \phi} \frac{\partial}{\partial \phi} \left(\sin \phi \frac{\partial}{\partial \phi} \right) \quad (5.3.15)$$

Let us average this expression in ϕ and θ direction. Then the two integrals that contain ϕ and θ derivatives vanish. The only remaining term is the one with the r derivative. Therefore, the cusp conditions for the spherical $\langle \psi \rangle_S$ average read

$$-\frac{1}{2\mu\psi} \frac{1}{r^2} \frac{\partial}{\partial r} \left(r^2 \frac{\partial}{\partial r} \right) \langle \psi \rangle_S + \frac{q_1 q_2}{r} \langle \psi \rangle_S < \infty \quad (5.3.16)$$

We can expand the spherical average of wave function in the Taylor series around the center of mass.

$$\langle \psi \rangle_S = c_0 + c_1 r + c_2 r^2 + \dots \quad (5.3.17)$$

Using this expansion, and imposing that the whole expression should be equal to 0, the cusp condition may be written as

$$c_1 = \mu q_1 q_2 c_0, \quad (5.3.18)$$

which, for electrons, gives us the cusp condition

$$c_1 = \frac{1}{2} c_0. \quad (5.3.19)$$

A similar reasoning may be applied to derive the electron-ion cusp condition,

$$c_1 = -Z c_0, \quad (5.3.20)$$

where Z is the atomic number of the ion.

5.3.2 Diffusion Quantum Monte Carlo

Variational Quantum Monte Carlo is limited by the chosen form of a wave function. To overcome, at least partially, this difficulty, we will use the Diffusion Quantum Monte Carlo method.

Let us begin with writing the Schrödinger equation in imaginary time. We make a substitution $\tau = it$, and the Schrödinger equation becomes:

$$-\frac{\partial}{\partial \tau} |\psi(\tau)\rangle = H |\psi(\tau)\rangle. \quad (5.3.21)$$

The general solution of this equation is:

$$|\psi(\tau)\rangle = e^{-H(\tau-\tau_0)} |\psi(x, \tau_0)\rangle. \quad (5.3.22)$$

Let us decompose the operator exponentials in the basis of energy eigenstates

$$|\psi(\tau)\rangle = \sum_i |i\rangle e^{-E_i(\tau-\tau_0)} \langle i|\psi(\tau_0)\rangle. \quad (5.3.23)$$

From this form it can be seen that the solution is following:

- Decreasing exponentially to 0, when all the eigenvalues are positive. The lowest energy component is decreasing most slowly. Therefore, if we carry on the imaginary time evolution long enough, the wavefunction will consist only of the ground state eigenfunction component, up to a constant, assuming that initial distribution has nonzero overlap with this eigenstate ($\langle i|\psi(x,0)\rangle$ should be nonzero).
- Increasing exponentially, when there are positive eigenvalues.
- Tending to lowest energy eigenstate, if the lowest eigenstate is zero (and $\langle i|\psi(x,0)\rangle \neq 0$).

The most desirable case for simulation is the third one. This might sound as if the method was useful only for a very limited case of systems, i.e. those with ground state with zero energy. However, we can just shift all the spectrum by a constant value E_T , subtracting this value from Hamiltonian. Then the evolution equation is simply

$$|\psi(\tau)\rangle = \sum_i |i\rangle e^{-(E_i-E_T)(\tau-\tau_0)} \langle i|\psi(\tau_0)\rangle. \quad (5.3.24)$$

If we could find a way to find a value of E_T which is equal to the energy of the lowest eigenstate, then the evolution will proceed as we want it to. Of course, we cannot do it "directly", because we do not know the ground state energy. It is one of the things that we want to compute.

But first - we still do not know how to simulate the time evolution. To get the idea, let us first look at the imaginary time Schrödinger equation of a free particle

$$\frac{\partial}{\partial \tau} \psi(x, \tau) = \frac{\nabla^2}{2} \psi(x, \tau), \quad (5.3.25)$$

where we put $m = 0$ to make expression clearer. We can write the general solution of Eq. 5.3.21 in position representation

$$\langle x | \psi(\tau) \rangle = \int \langle x | e^{-H(\tau-\tau_0)} | y \rangle \langle y | \psi(\tau_0) \rangle dy, \quad (5.3.26)$$

The function

$$G(\tau - \tau_0, x, y) = \int \langle x | e^{-H(\tau-\tau_0)} | y \rangle, \quad (5.3.27)$$

called Green's function, describes the time evolution of a Dirac delta. Every point of the initial wave function evolves according to $G(\tau, x, y)$, so the position integral gives the summaric contribution of all the points.

For the diffusion equation, the Green's function is

$$\begin{aligned} \langle x | e^{-\frac{\nabla^2}{2} \tau} | y \rangle &= \int \langle x | p \rangle \langle p | e^{-\frac{\nabla^2}{2} \tau} | p' \rangle \langle p' | y \rangle dp dp' = \int \langle x | p \rangle e^{-\frac{p^2}{2} \tau} \langle p | p' \rangle \langle p' | y \rangle dp dp' = \\ &= \frac{1}{2\pi} \int e^{-\frac{p^2}{2} \tau + i p(x-y)} dp = \frac{1}{2\pi} e^{-\frac{(x-y)^2}{2\tau}} \int e^{-((\frac{p}{\sqrt{2}}\sqrt{\tau})^2 + i(y-x)p - \frac{(x-y)^2}{2\tau})} dp = \\ &= \frac{1}{\sqrt{2\pi\tau}} e^{-\frac{(x-y)^2}{2\tau}}, \end{aligned} \quad (5.3.28)$$

where we inserted two times the identity operator in the basis of the momentum eigenstates, and used the position representation of momentum eigenstates $\langle x | p \rangle = 1/(2\pi) e^{ipx}$.

The diffusion equation has probabilistic interpretation in terms of random walks. It describes the time evolution of probability density of a random walker position. We can construct such a random walk using Green's function $G(\tau, x, y)$ as a transition probability of a random walker from y to x in time τ . We will take discrete and equal time steps, therefore, because the Green's function depends only on the time difference, this probability distribution will be the same on every step.

Having a large ensemble of walkers, we can approximate the wave function by a histogram of their density. We must of course assume that the wave function is non-negative in all the domain (the case of wave functions that change signs will be mentioned later).

Unfortunately, the wave function of a free particle, which is distributed all through the space, so it will be not approximated well by finite number of walkers. But a similar procedure can be used for the case with a potential.

First of all, we should split the exponential into exponentials of kinetic and potential energy parts. Because in general they do not commute, we will use the Trotter-Suzuki formula

$$e^{(A+B)} = \lim_{n \rightarrow \infty} (e^{\frac{A}{n}} e^{\frac{B}{n}})^n. \quad (5.3.29)$$

For our case

$$e^{-K\tau - (V(x) - E_T)\tau} = \lim_{n \rightarrow \infty} (e^{-K\frac{\tau}{n}} e^{-(V(x) - E_T)\frac{\tau}{n}})^n, \quad (5.3.30)$$

where K is the kinetic energy operator, and $V(x)$ is the potential, describing both interactions and external potential. In our numerical simulations, we do not go with the limit to infinity, we just use this equation as an approximation valid for large number of time steps. The Green's function for long times τ may be therefore approximated by acting on a wavefunction n times with short-time Green's function $e^{-\frac{\nabla^2}{2}\frac{\tau}{n}} e^{-(V(x) - E_T)\frac{\tau}{n}}$. For the approximation to be good, the time step $\frac{\tau}{n}$ should be as small as possible.

Now, the short-time approximation to Green's function consists of two parts: the first is exactly the same as in the free-particle case (except that we can have many particles with different masses), and the second is exponent of a function $V(x) - E_T$, not an operator.

It is important to note that in general the Green's function does not conserve norm, so in general the solution of the imaginary time Schrödinger equation cannot be treated as a probability distribution. But still we can think in terms of density of walkers (which will approximate the unnormalized wavefunction). The lack of norm conserving means that the number of walkers change - we will turn to so-called branching random walk (Fig. 5.1). The first part, however, is norm-conserving. One walk step will then consist of

- *Diffusion step* - the walkers are moved with probability given by the kinetic part
- *Branching step* - the number of walkers is changed. Let us define $q = e^{-(V(x) - E_T)\frac{\tau}{n}}$ where x is the position of chosen walker. Then, if $q < 1$, the walker is "killed" with probability $1 - q$ and "stays alive" with probability q . If $q > 1$ new walkers are produced: $\lfloor q \rfloor$ with probability $q - \lfloor q \rfloor$ and $\lfloor q \rfloor - 1$ with probability $1 - q + \lfloor q \rfloor$.

Now one question remains - how to find E_T to ensure the convergence of the density to the ground state wave function. We know that when $E_0 - E_T > 0$ the wave function - and so, the number of walkers, is decreasing. When $E_0 - E_T < 0$ it is increased. So, we might just keep track of the number of walkers, and then increase or decrease E_T depending on whether the number of walkers is higher or lower than desired. For example, we can use

$$E_T = \langle V(\vec{r}) \rangle + \ln\left(\frac{\tilde{M}}{M}\right), \quad (5.3.31)$$

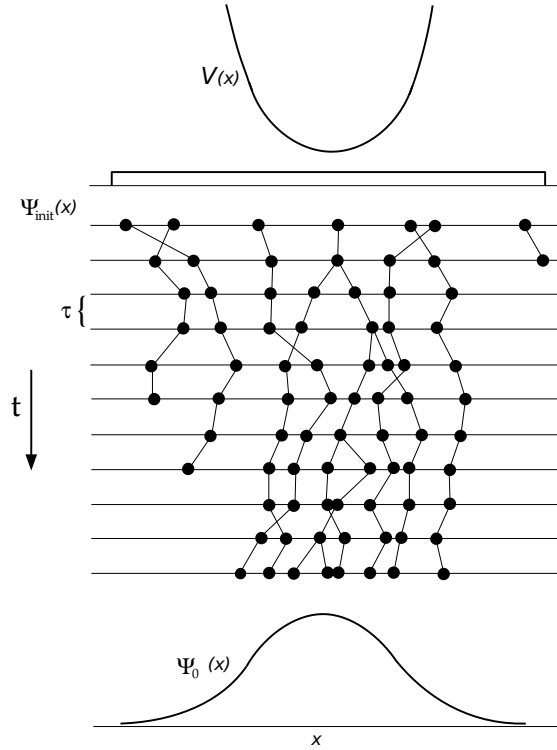


FIGURE 5.1: The idea of the DMC method. The walkers make both diffusion and branching steps. High potential "kills" walkers, while the low potential multiplies them. Reprinted from [51]

where \tilde{M} is the desired number of walkers and M is the number of walkers in current move. $\langle V(x) \rangle$ is the arithmetic average of the potential sampled at all walkers' positions in the move.

The above DMC algorithm is correct, but it suffers from two disadvantages.

- In the regions of very high negative potentials the production of walkers is very high and may lead to population explosion. This is important especially in the case of Coulomb potential, which diverges when r tends to 0.
- The wave function can only be positive. That means that, so far, we have no idea of how to perform DMC calculations of fermions, which makes this method completely useless in quantum chemistry.

The first problem resembles the problem with Monte Carlo integration using uniform distribution. The solution is also similar: importance sampling.

Let us write the equation for a new function

$$\rho(x, \tau) = \psi(x, \tau) \psi_T(x), \quad (5.3.32)$$

where $\psi_T(x)$ is a trial function, an initial guess hopefully resembling the ground state.

The Schrödinger equation can be written as

$$\frac{\partial}{\partial \tau} \rho(x, \tau) = \frac{1}{2} \nabla (\nabla - F(x)) \rho(x, \tau) - (E_L(x) - E_T) \rho(x, \tau), \quad (5.3.33)$$

where

$$F(x) = \frac{2 \nabla \psi_T(x)}{\psi_T(x)} \quad (5.3.34)$$

and

$$E_L(x) = \frac{\frac{-\nabla \psi_T(x)}{2} + V(x)}{\psi_T(x)} \quad (5.3.35)$$

Again, we can make a division into diffusion and branching steps. The diffusion Green's function now read:

$$G(x, y, \Delta \tau) = \frac{1}{2\pi\Delta\tau} e^{-\frac{(y-x-F(x)\Delta\tau/2)^2}{2\Delta\tau}} \quad (5.3.36)$$

The movement of a walker according to this Green's function is again according to normal distribution of variance τ , but its mean is shifted by $F(x)\Delta\tau/2$. Therefore the position of the walker in next iteration can be written as

$$x(\tau + \Delta\tau) = x(\tau) + F(x(\tau))\Delta\tau/2 + \eta\sqrt{\Delta\tau}, \quad (5.3.37)$$

where η is drawn randomly from Gaussian distribution of mean 0 and variance 1. The branching step is also similar to the previously described, although now the population change is described by

$$q = e^{-\Delta\tau(E_L(x) - E_T)}. \quad (5.3.38)$$

The Green's function 5.3.36 is only an approximation up to first order in $\Delta\tau$. Using this function we will receive an additional time-step bias. We can get rid of it using an additional Metropolis acceptance-rejection step.

The usage of guiding function allows also to solve the "fermion problem". The trial wave function has a nodal surface, where it changes sign. We can demand that the diffusion steps in which the wavefunction changes sign, are not accepted, separating the calculation into regions of positive and negative wavefunction.

This make the fermion calculation less accurate than boson ones, because the nodal surface cannot be optimized, it is the same that in the trial wavefunction. Therefore DMC results are "as good as the nodes". The trial functions, in our case, are the optimized ground state wave function from the VMC calculations.

Chapter 6

Results

In the following chapter, we will present our results. It will be divided in two sections. First, we will investigate the effect of disorder, using the lattice models: tight binding and Hubbard. Then, we use Quantum Monte Carlo to look into the effect of electronic correlation in clean system.

6.1 The effects of disorder

6.1.1 One-electron properties

We begin with the investigation of the effect of disorder on band structure and density of states of graphene quantum dots in one-electron approximation. We take under consideration the three structures described in Chapter 2: armchair hexagon, zigzag hexagon and zigzag triangle, reflecting different classes of graphene quantum dots. The number of atoms in every structure is around 1000 (1014 for hexagons and 1021 for the triangle). We use the tight-binding model which was described all throughout this thesis. We use the first- and second- neighbours integrals, the former equal $t = -2.84eV$ and the latter $t_2 = 0.1eV$. The disorder is modelled by Anderson model, described in sec. 4. The Hamiltonian of disordered system is

$$H_{TB} + H_{dis}, \quad (6.1.1)$$

where

$$H_{dis} = \sum_i \varepsilon_i c_i^\dagger c_i, \quad (6.1.2)$$

and ε_i 's are drawn randomly from uniform distribution on $[-W/2, W/2]$.

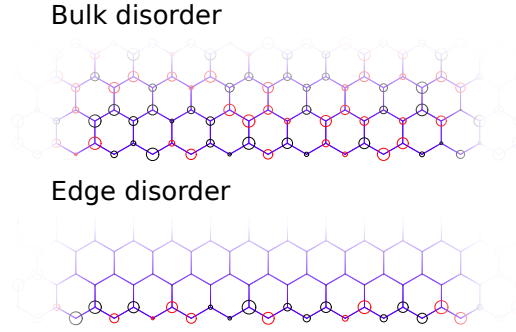


FIGURE 6.1: Examples of bulk and edge disorder. The areas of the circles are proportional to ϵ_i 's, and red and black is for positive and negative ϵ_i , respectively

We make calculations for both edge and bulk disorder (see Fig. 6.1 to see how "edge" is defined). The Hamiltonian matrices are diagonalized using Eigen C++ library.

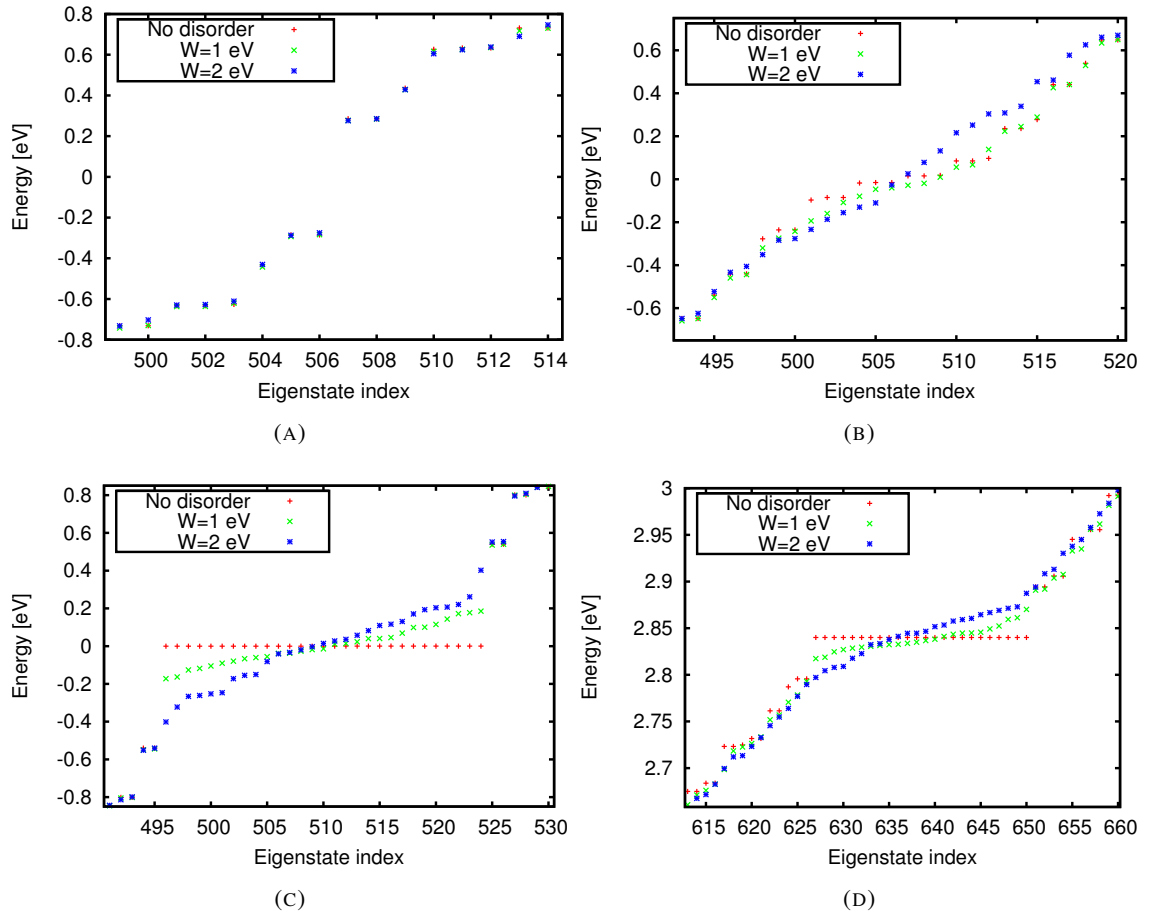


FIGURE 6.2: Comparison of tight-binding energy spectra for clean and edge-disordered dots. A)-C) show the vicinity of Fermi level for: A) armchair hexagon, B) zigzag hexagon C) zigzag triangle, composed of approx. 1000 atoms. D) show the van Hove singularity region for the armchair hexagon.

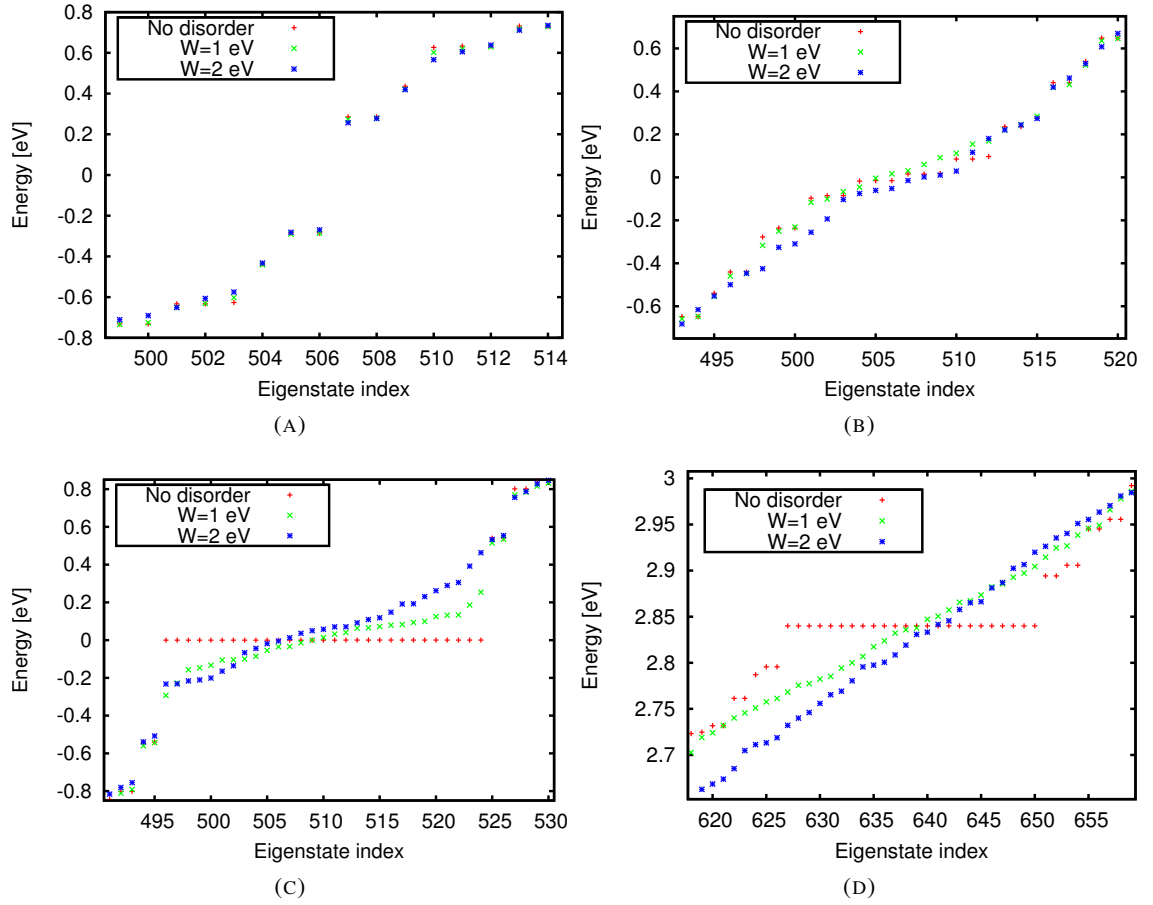


FIGURE 6.3: Comparison of tight-binding energy spectra for clean and bulk-disordered dots. A)-B) show the vicinity of Fermi level for: A) armchair hexagon, B) zigzag hexagon C) zigzag triangle, composed of approx. 1000 atoms. D) show the van Hove singularity region for the armchair hexagon.

Figures 6.2 and 6.3 show example energy spectra for these three structures, for $W = 2 \text{ eV}$. Fig. 6.4 shows the averaged density of states. As in chapter 3, the DOS is approximated by a convolution of the spectrum with Gaussian kernel with standard deviation $\xi = 0.16 \text{ eV}$. We average this density of states over 5000 different, random disorder configurations.

Clearly, there are two regions in which the disorder effect seems highest: the van Hove singularities and the edge state peak. The former is influenced much stronger by bulk disorder while the latter is affected by both forms of disorder in similar way.

This can be understood knowing that the edge states are, as the name suggest, localized at the edges, so the variation of on-site energy at the other sites is not significant. The opposite happens in the case of van Hove singularity region, where most of the electronic density is localized at the center, so the effect of edge on-site energy variation is not so clearly seen. The individual energy levels, although, are also broadened in the other areas of the spectrum. This broadening is bigger in the case of bulk disorder. This effect may be seen if the Gaussian half-width would be lower.

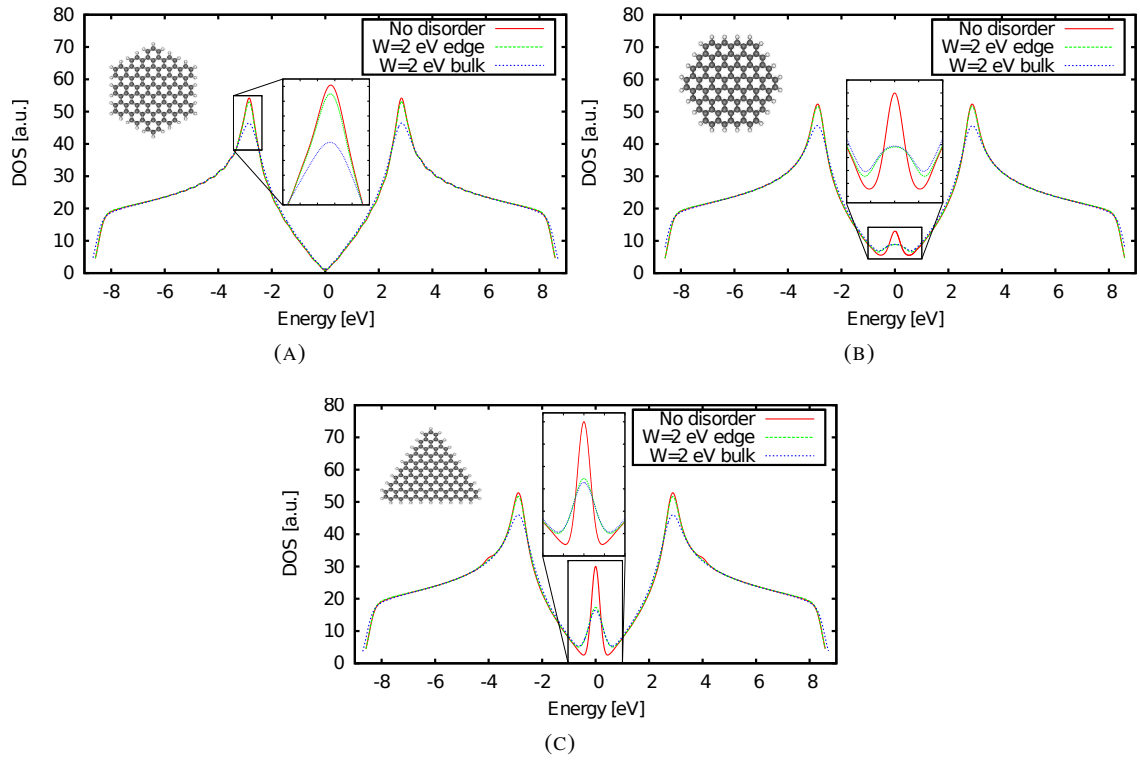


FIGURE 6.4: Comparison of density of states for A) armchair hexagon, B) zigzag hexagon, C) zigzag triangle, for bulk and edge disorder. Insets show the smaller structures of given shape and edge type.

6.1.2 A geometry for single zigzag edge investigation

Secondly, we want to study the edge states localized at one zigzag edge. Therefore, we choose another shape of a quantum dot - a pentagon with one zigzag edge and four armchair ones (see e.g. Fig. 6.5). We hope that this geometry is a representative example of a whole class of quantum dots. The only characteristic is the length of zigzag edge, the fact that there is only one such edge, and that the number of atoms is sufficiently low. That happens because:

- We are interested only in the region around Fermi level, because we keep our focus on the low-energy properties.
- If there would be more zigzag edges, the edge states may overlap and the eigenstates may be a mixture of them. If there is only one edge, we are sure that they are localized on it.
- The armchair edge does not introduce sublattice imbalance and in consequence edge states. So that, no matter what "happens" far from the zigzag edge, as long as no other zigzag fragments are introduced, the sublattice imbalance remains constant and low energy electronic properties are not affected.

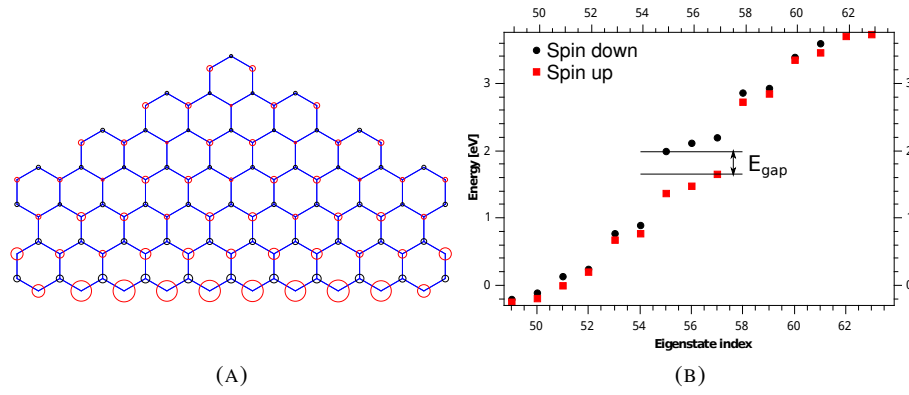


FIGURE 6.5: Magnetism in pentagonal quantum dot with one zigzag edge and $N_{deg} = 3$, A) Spin density (the area of circles is proportional to $|\langle n_{\uparrow} \rangle - \langle n_{\downarrow} \rangle|$, with red corresponding to positive, and right to negative values), B) Hubbard spectrum.

- The energy gap separating the edge states from the rest of the spectrum is decreasing with atom number. For structures with large number of atoms, the conduction and valence bands overlap with edge states, and it can influence their behaviour.

To the degree of generalization described before, we can say that we research the properties of a single zigzag edge, not a given structure.

To satisfy the requirements of the geometry, the number of edge atoms N_{edge} , defined as the number of atoms with two nearest neighbours, should be

$$N_{edge} = 3n + 1, \quad (6.1.3)$$

where n is an integer. Other values of N_{edge} will lead to existence of other zigzag fragments, which we do not want at this moment. We notice that n is equal to the number of degenerate states in the zero-energy shell N_{deg} .

6.1.3 Magnetism of a single zigzag edge

We investigate the magnetic properties of a single zigzag edge using the Hubbard model. We investigate four different edge lengths, corresponding to $N_{deg} = 3, 4, 5, 6$ degenerate states. We use the mean-field SCF approach described in Chapter 5. As stated in Chapter 3, we are interested only in charge-neutral systems because their correlations are weak enough to make the mean-field Hubbard model a reasonable approximation. Because the zero-energy shell is well-separated from the rest, the excitation of an electron from the gap is too expensive energetically, and the occupations may vary only inside the shell. The number of available total spin values is reduced to a small number. The maximal total spin is $N_{deg}/2$, and the possible total spin values vary by one, because of charge neutrality requirement. The Hamiltonian matrices are diagonalized using Eigen library. The convergence criterion is $\Delta E < 10^{-7}$ eV. The convergence takes

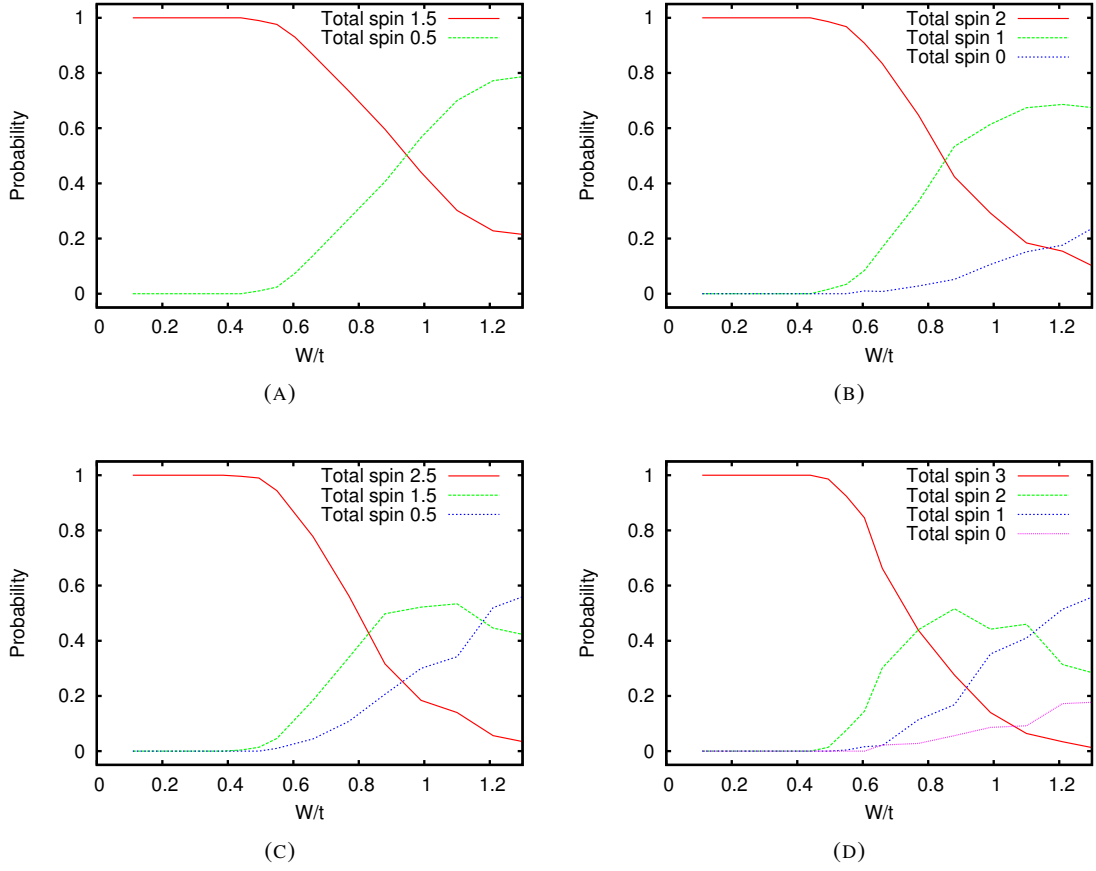


FIGURE 6.6: Probabilities that the ground state has given spin, for A) $N_{deg} = 3$, B) $N_{deg} = 4$, C) $N_{deg} = 5$, D) $N_{deg} = 6$, with edge disorder.

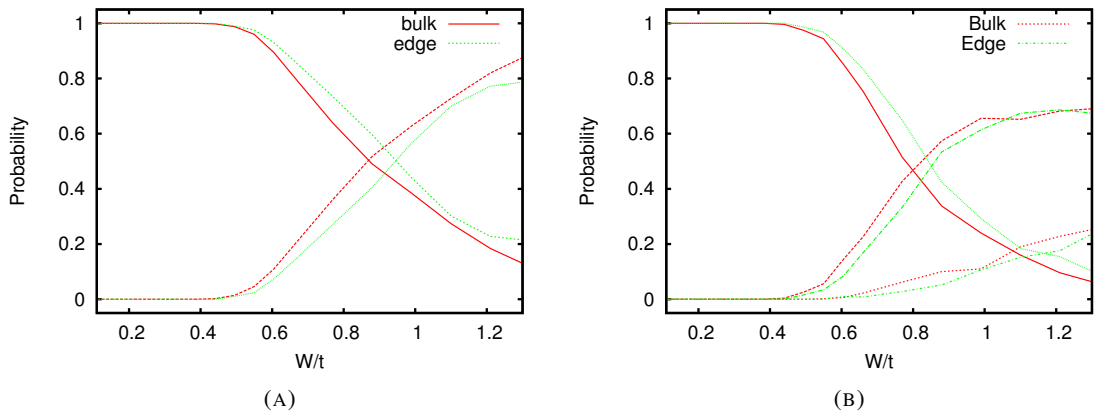


FIGURE 6.7: Probabilities that the ground state has given spin - comparison of bulk and edge disorder effect. a) $N_{deg} = 3$, b) $N_{deg} = 4$.

usually a few tens of iterations, so it is considerably slower than the tight-binding. Therefore we take 500 realizations of disorder for each value of total spin. For total spin 0, the calculation often do not converge, and "jumps" between a set of states. But, for the calculations here, this often has no effect, because often other states have energies higher than the maximum of the ground state variation. The few cases when they do not the calculation is performed again for other random configuration.

Without disorder, all these structures are maximally spin polarized, in agreement with the Lieb's theorem (Fig. 6.5). If we introduce the disorder, the dispersion of the edge states begin to grow. Because disorder breaks the sublattice symmetry, the Lieb's theorem no longer applies. so there is no reason that the structure should remain fully polarized.

Figure 6.6 shows the probability that given structure has total spin S at given value of disorder strength. These probabilities are simply the fractions of the number of disorder configurations that have the given spin of ground state to the number of all configurations. In our case the calculation is done for 500 configurations.

For all four zigzag edge lengths, the probabilities show similar behaviour. There is a plateau of maximal polarization for sufficiently small disorder strength. After a certain "breakdown value" the probability of this maximal polarization falls, and another values of total spin appear, but, (except from $N_{deg} = 3$ when there is no other way), the probability of the complete depolarization is still low - and increases with the further increase of disorder.

The "breakdown value" of disorder strength differs between the zigzag edge lengths, although it oscillates around $W/t \approx 0.45$, with $W/t \approx 0.45$ for $N_{deg} = 3, 6$, $W/t \approx 0.5$ for $N_{deg} = 4$, and $W/t \approx 0.39$ for $N_{deg} = 5$.

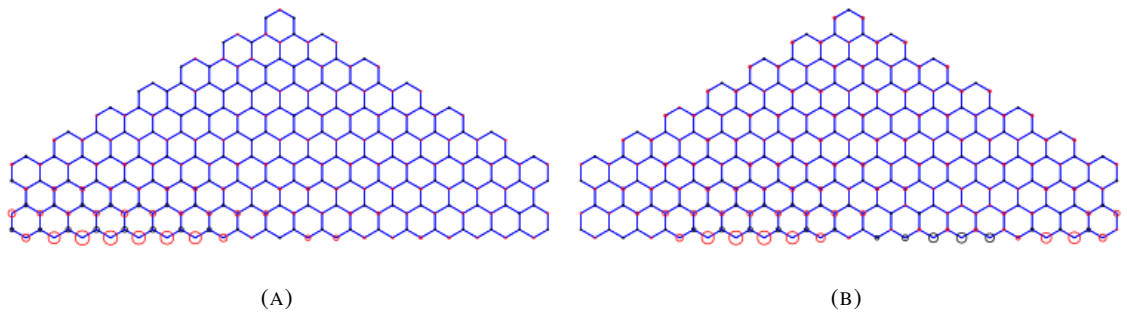


FIGURE 6.8: Two examples of spin density for $N_{deg} = 6$ and total spin 1 ($W/t \approx 1.1$).

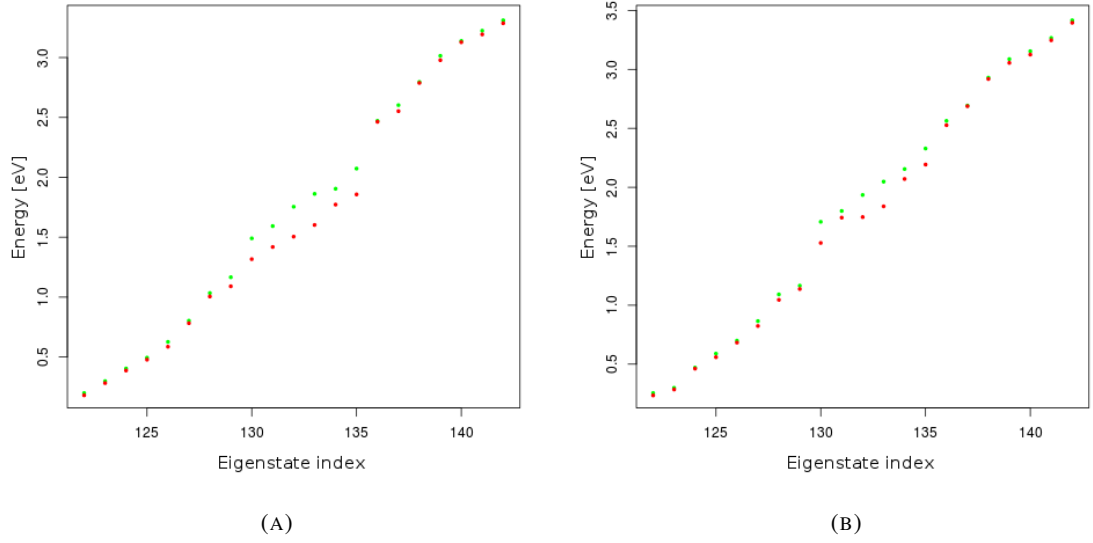


FIGURE 6.9: The mean-field Hubbard energy spectra corresponding to spin densities from Fig. 6.8.

These results are obtained for edge disorder. Similar calculations were done for bulk disorder for $n = 3, 4$. The comparison of these two is shown in Fig. 6.7. The shape of the curves is similar, although it is seen that for the bulk disorder the magnetization falls slightly faster. This can be easily explained, as the edge states are mostly concentrated within the region of edge disorder, but their exponential tails spread into the bulk - so the difference comes from the action of disorder onto these tails.

The examples of spin densities and the corresponding Hubbard energy spectra, are shown in figures 6.8, 6.9, 6.10 and 6.11. The breaking of sublattice symmetry manifest itself also in magnetization - now both signs of average spin can be present on the same sublattice. The energy spectra show the increased dispersion of the zero-energy shell.

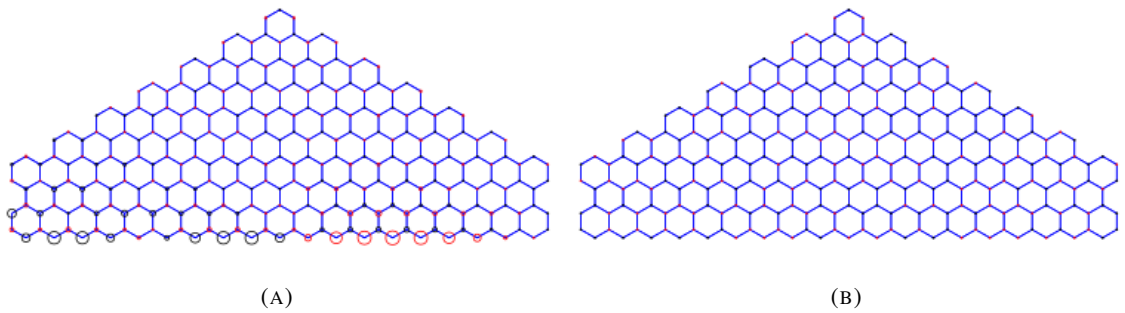


FIGURE 6.10: Two examples of spin density for $N_{deg} = 6$ and total spin 0 ($W/t \approx 1.1$)

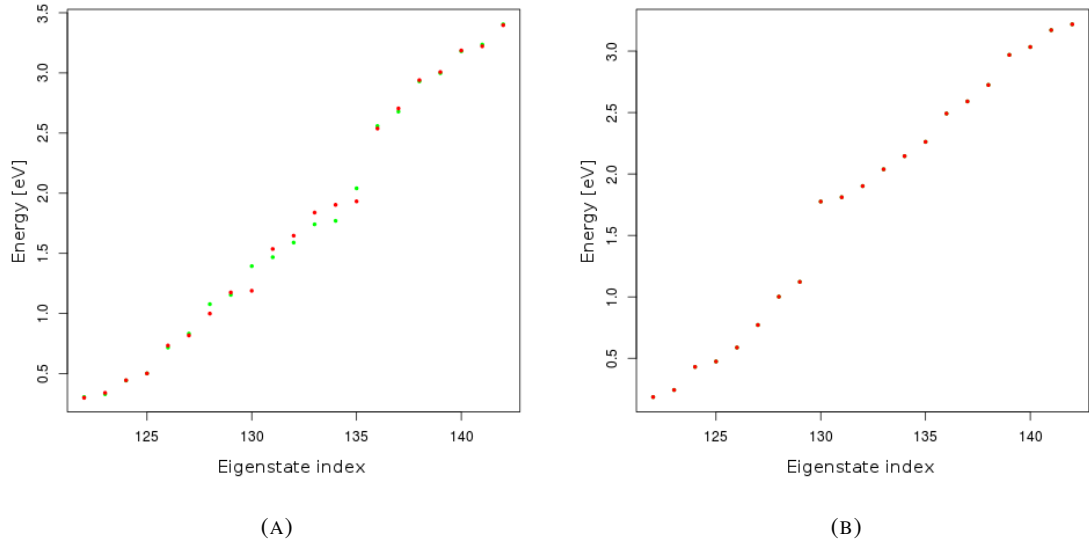


FIGURE 6.11: The mean-field Hubbard energy spectra corresponding to spin densities from Fig. 6.10

6.2 Correlations: Quantum Monte Carlo

We used the Quantum Monte Carlo methods to investigate two smallest graphene quantum dots of the shape of zigzag triangle, made of 13 and 22 carbon atoms (Fig. 6.12). The calculations were done using CASINO software [54].

The trial wavefunction was generated with restricted and restricted open-shell Hartree-Fock method (22 C atoms) or DFT method (13 C atoms), in both cases using Gaussian software [56]. The PBE exchange-correlation functional was used in the latter, following [57]. 6-311G Gaussian basis was used. The geometry was optimized separately for all values of total spin. For both structures, we investigate the charge neutral systems only.

6.2.1 Calculation details

CASINO software allows to choose three methods: energy (emin), variance (varmin) and mean absolute deviation (madmin) minimization. The form of Jastrow factors allows to vary expansion order, cutoff lengths, number of continuous derivatives at cutoff and spin dependence of expansion coefficients. We tried four Jastrow factors, involving only functions u and χ (see chapter 4), differing by spin dependence. u is electron-electron term, so it has two spin arguments and in

6.2.2 Results

We begin from the triangle made of 13 carbon atoms. This structure has $N_{deg} = 1$, so we have to investigate only one spin configuration - one electron on one zero energy state. The results are seen in table 6.1. It can be seen that the value of total energy is dependent on method - the varmin and madmin methods seem to give similar results, while the emin gives energy lower than these two. The emin method, although, needs more optimization steps - in varmin and madmin usually only the first steps give the significant lowering of energy (see Fig.6.13). We used 5 or 10 optimization steps for varmin and madmin and 15 for emin. The number of used VMC iterations differ because sometimes with 100000 there were warnings about poor convergence, or the u function from Jastrow was not monotonic, which indicates poor optimization. In such cases we used 200000 or 500000.

All the resulting VMC energies are higher than the DFT result for an initial guess. The reason is that even with the same orbitals DFT calculates the energy in different way than QMC. The results show that for this system the DFT method includes correlation to better extent than VMC, at least within the parameters we tried.

Four VMC runs were continued using DMC. The resulting energies are lower than those obtained using DFT, showing that the correlations are included to better extent. But it should be noted that the DMC results are only preliminary. The DMC runs were not long enough to capture the proper statistics, so the energies and especially the error bars are not reliable. Also, the proper DMC procedure requires to perform several calculations with different time steps and extrapolate to zero time steps. This would allow to get rid of the time step error, resulting from the short-time approximation for the Green's function.

TABLE 6.2: QMC and Hartree-Fock results for the 22-C-atom triangle.

QMC								
Spin dependence	Optimization method	DMC equil. iterations	DMC accum. iterations	Spin	VMC energy [a.u.]	VMC error [a.u.]	DMC energy [a.u.]	DMC error [a.u.]
1	varmin			$\uparrow\uparrow$	-842.603	0.009		
				$\uparrow\downarrow$	-841.987	0.009		
				gap	0.616			
2	varmin	20000	410000	$\uparrow\uparrow$	-842.764	0.009	-845.27	0.04
		20000	89000	$\uparrow\downarrow$	-842.05	0.02	-845.17	0.06
				gap	0.71		0.010	
Hartree-Fock								
Spin	Energy							
$\uparrow\uparrow$	-839.906							
$\uparrow\downarrow$	-839.959							
Gap	0.053							

The next structure - 22 carbon atom triangle - has two zero-energy states, so it allows to investigate the magnetism. We can populate the zero-energy shell with two electrons, which gives

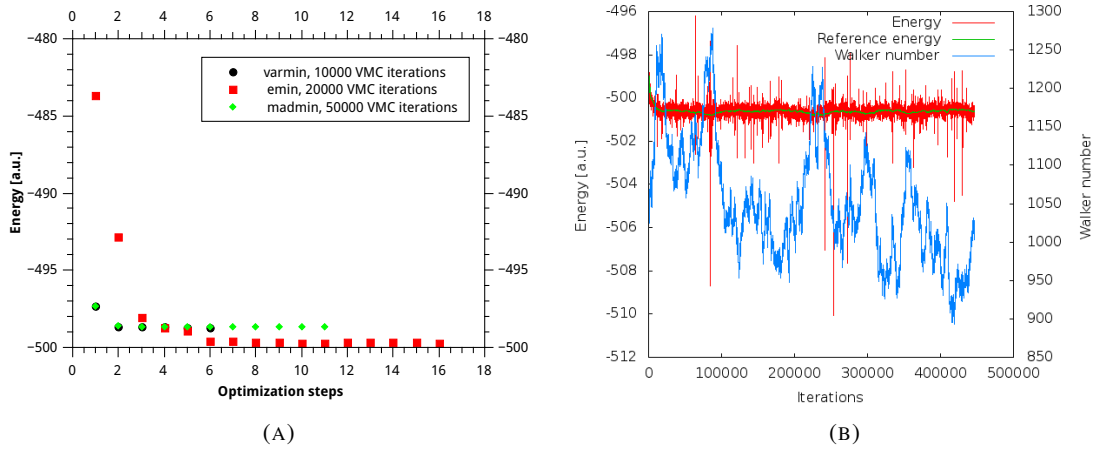


FIGURE 6.13: a) The energy optimization process for 13-C-atom triangle for 2nd spin dependence variant. b) The walker population, energy and reference energy for the DMC run starting from variance-optimized spin-independent Jastrow factor, for triangle of 13 carbon atoms

us two possible total spin values: $S = 0$ (parallel spins) and $S = 1$ (antiparallel spins). Table 6.2 shows our results. We compared two variants of Jastrow factor's spin dependence. We used the varmin method with and 10 optimization steps and 500000 VMC iterations at every step. The ground state is $S = 1$, so the Lieb's theorem results are confirmed, in agreement with [26]. The energies are lowered by 0.23 – 0.34% by the VMC method (comparing to the Hartree-Fock result). The spin gaps are an order of magnitude larger than in Hartree-Fock.

For one of the optimized Jastrow factors we performed the preliminary DMC runs, which show that the spin gap decreases - now it is about two times greater than in Hartree-Fock. Also, it results in further decrease of energy, the result of DMC calculation is 0.63 – 0.64% lower than the Hartree-Fock energy. These results, although, need to be treated with caution, because the runs were too short to accumulate the proper statistics. Also, the extrapolation to zero time-step needs to be performed to increase accuracy and reliability.

Chapter 7

Summary and conclusions

In this thesis we investigated the electronic and magnetic properties of graphene quantum dots, including the effect of disorder and correlations. The so-called zigzag edges of these structures host the edge states. When the sublattice imbalance is non-zero, these states form a degenerate shell at the Fermi level, which leads to appearance of finite magnetic moment.

We investigated the influence of model short-range disorder on the electronic and magnetic properties of these systems. We found that the disorder effect on the average density of states is mostly smearing the sharp peaks: the van Hove singularities and the edge state peak. The latter is smeared to similar degree by both edge and bulk onsite energy variation, while on the former the bulk disorder acts much stronger than the edge. As for magnetic properties, we found that the magnetization is not decaying monotonously with increasing disorder strength. Instead, it has a plateau in which it is stable.

The correlations were investigated by VMC (Variational Monte Carlo) and DMC (Diffusion Monte Carlo) methods. We observed the lowering of energy resulting from VMC calculation compared to Hartree-Fock, of about 0.2 – 0.3% and subsequent lowering of DMC energy (about 0.6% compared to Hartree-Fock). The magnetization of charge-neutral structures behaved according to predictions from Hubbard model and other methods. The spin gap of the 22-atom triangle grew an order of magnitude higher in VMC comparing to Hartree-Fock and two times in DMC, comparing to Hartree-Fock.

These results are just a starting point for investigating the graphene nanostructures using QMC. The longer DMC runs must be performed to reach the reliable statistics. Then, other runs with different time steps must be performed to avoid the time-step error. When this is done, various Jastrow factors (e.g. differing by expansion order) may be investigated to find the one that describes the correlations most accurately.

The next step would be the investigation of charged structures. It may for example allow to investigate the depolarization effect, which was seen in the configuration-interaction calculations of triangular graphene quantum dots with one additional electron. [\[30\]](#).

Bibliography

- [1] Nobelprize.org, “The Nobel prize in physics 2010 - advanced information.” http://www.nobelprize.org/nobel_prizes/physics/laureates/2010/advanced.html, June 2013.
- [2] N. O. Weiss, H. Zhou, L. Liao, Y. Liu, S. Jiang, Y. Huang, and X. Duan, “Graphene: an emerging electronic material.,” *Adv. Mater. Weinheim*, vol. 24, no. 43, pp. 5782–825, 2012.
- [3] F. Schwierz, “Graphene transistors,” *Nature Nanotechnology*, vol. 5, p. 487–496, 2010.
- [4] Y.-M. Lin, A. Valdes-Garcia, S.-J. Han, D. B. Farmer, I. Meric, Y. Sun, Y. Wu, C. Dimitrakopoulos, A. Grill, P. Avouris, and K. A. Jenkins, “Wafer-scale graphene integrated circuit,” *Science*, vol. 332, no. 6035, pp. 1294–1297, 2011.
- [5] D. S. Hecht, L. Hu, and G. Irvin, “Emerging transparent electrodes based on thin films of carbon nanotubes, graphene, and metallic nanostructures,” *Advanced Materials*, vol. 23, no. 13, pp. 1482–1513, 2011.
- [6] S. Bae, H. Kim, Y. Lee, X. Xu, J.-S. Park, Y. Zheng, J. Balakrishnan, T. Lei, H. Ri Kim, Y. I. Song, Y.-J. Kim, K. S. Kim, B. Ozyilmaz, J.-H. Ahn, B. H. Hong, and S. Iijima, “Roll-to-roll production of 30-inch graphene films for transparent electrodes,” *Nat Nano*, vol. 5, pp. 574–578, Aug 2010.
- [7] F. Bonaccorso, Z. Sun, T. Hasan, and A. C. Ferrari, “Graphene photonics and optoelectronics,” *Nature Photonics*, vol. 4, pp. 611 – 622, 2010.
- [8] X. Huang, X. Qi, F. Boey, and H. Zhang, “Graphene-based composites,” *Chem. Soc. Rev.*, vol. 41, pp. 666–686, 2012.
- [9] F. Schedin, A. K. Geim, S. V. Morozov, E. W. Hill, P. Blake, M. I. Katsnelson, and K. S. Novoselov, “Detection of individual gas molecules adsorbed on graphene,” *Nat Mater*, vol. 6, pp. 652–655, Sep 2007.
- [10] bbc.co.uk, “Miracle material graphene can distil booze, says study.” <http://www.bbc.co.uk/news/science-environment-16747208>, January 2012.

- [11] R. R. Nair, H. A. Wu, P. N. Jayaram, I. V. Grigorieva, and A. K. Geim, “Unimpeded permeation of water through helium-leak-tight graphene-based membranes,” *Science*, vol. 335, no. 6067, pp. 442–444, 2012.
- [12] K. S. Novoselov, A. K. Geim, S. V. Morozov, D. Jiang, Y. Zhang, S. V. Dubonos, I. V. Grigorieva, and A. A. Firsov, “Electric field effect in atomically thin carbon films,” *Science*, vol. 306, pp. 666–669, oct 2004.
- [13] K. S. Novoselov, A. K. Geim, S. V. Morozov, D. Jiang, M. I. Katsnelson, S. V. Dubonos, and A. A. Firsov, “Two-dimensional gas of massless dirac fermions in graphene,” *Nature*, vol. 438, pp. 197–200, 2005.
- [14] M. J. Allen, V. C. Tung, and R. B. Kaner, “Honeycomb carbon: A review of graphene,” *Chemical Reviews*, vol. 110, no. 1, pp. 132–145, 2010. PMID: 19610631.
- [15] P. R. Wallace, “The band theory of graphite,” *Phys. Rev.*, vol. 71, pp. 622–634, May 1947.
- [16] S. Reich, J. Maultzsch, C. Thomsen, and P. Ordejón, “Tight-binding description of graphene,” *Phys. Rev. B*, vol. 66, p. 035412, Jul 2002.
- [17] R. Saito, G. Dresselhaus, and M. S. Dresselhaus, *Physical Properties of Carbon Nanotubes*. World Scientific Publishing, 1998. ISBN 978-1-86094-093-4 (hb) ISBN 978-1-86094-223-5 (pb).
- [18] A. H. Castro Neto, F. Guinea, N. M. R. Peres, K. S. Novoselov, and A. K. Geim, “The electronic properties of graphene,” *Reviews of Modern Physics*, vol. 81, pp. 109–162, jan 2009.
- [19] G. W. Semenoff, “Condensed-Matter Simulation of a Three-Dimensional Anomaly,” *Physical Review Letters*, vol. 53, pp. 2449–2452, Dec. 1984.
- [20] F. D. M. Haldane, “Model for a Quantum Hall Effect without Landau Levels: Condensed-Matter Realization of the ‘Parity Anomaly’,” *Phys. Rev. Lett.*, vol. 61, pp. 2015–2018, 1988.
- [21] L. Ci, Z. Xu, L. Wang, W. Gao, F. Ding, K. Kelly, B. Yakobson, and P. Ajayan, “Controlled nanocutting of graphene,” *Nano Research*, vol. 1, no. 2, pp. 116–122, 2008.
- [22] L. C. Campos, V. R. Manfrinato, J. D. Sanchez-Yamagishi, J. Kong, and P. Jarillo-Herrero, “Anisotropic etching and nanoribbon formation in single-layer graphene,” *Nano Letters*, vol. 9, no. 7, pp. 2600–2604, 2009. PMID: 19527022.
- [23] L. Zhi and K. Mullen, “A bottom-up approach from molecular nanographenes to unconventional carbon materials,” *J. Mater. Chem.*, vol. 18, pp. 1472–1484, 2008.

- [24] T. Yamamoto, T. Noguchi, and K. Watanabe, “Edge-state signature in optical absorption of nanographenes: Tight-binding method and time-dependent density functional theory calculations,” *Phys. Rev. B*, vol. 74, p. 121409, Sep 2006.
- [25] M. Ezawa, “Metallic graphene nanodisks: Electronic and magnetic properties,” *Phys. Rev. B*, vol. 76, p. 245415, Dec 2007.
- [26] J. Fernández-Rossier and J. J. Palacios, “Magnetism in graphene nanoislands,” *Phys. Rev. Lett.*, vol. 99, p. 177204, Oct 2007.
- [27] W. L. Wang, S. Meng, and E. Kaxiras, “Graphene nanoflakes with large spin,” *Nano Letters*, vol. 8, no. 1, pp. 241–245, 2008. PMID: 18052302.
- [28] Z. Z. Zhang, K. Chang, and F. M. Peeters, “Tuning of energy levels and optical properties of graphene quantum dots,” *Phys. Rev. B*, vol. 77, p. 235411, Jun 2008.
- [29] A. D. Güçlü, P. Potasz, O. Voznyy, M. Korkusinski, and P. Hawrylak, “Magnetism and correlations in fractionally filled degenerate shells of graphene quantum dots,” *Phys. Rev. Lett.*, vol. 103, p. 246805, Dec 2009.
- [30] P. Potasz, A. D. Güçlü, A. Wójs, and P. Hawrylak, “Electronic properties of gated triangular graphene quantum dots: Magnetism, correlations, and geometrical effects,” *Phys. Rev. B*, vol. 85, p. 075431, Feb 2012.
- [31] D. S. L. Abergel, V. Apalkov, J. Berashevich, K. Ziegler, and T. Chakraborty, “Properties of graphene: a theoretical perspective,” *Advances in Physics*, vol. 59, pp. 261–482, jul 2010.
- [32] Y. Kobayashi, K.-i. Fukui, T. Enoki, K. Kusakabe, and Y. Kaburagi, “Observation of zigzag and armchair edges of graphite using scanning tunneling microscopy and spectroscopy,” *Phys. Rev. B*, vol. 71, p. 193406, May 2005.
- [33] P. W. Brouwer, E. Racine, A. Furusaki, Y. Hatsugai, Y. Morita, and C. Mudry, “Zero modes in the random hopping model,” *Phys. Rev. B*, vol. 66, p. 014204, Jul 2002.
- [34] V. M. Pereira, J. M. B. Lopes dos Santos, and A. H. Castro Neto, “Modeling disorder in graphene,” *Phys. Rev. B*, vol. 77, p. 115109, Mar 2008.
- [35] E. H. Lieb, “Two theorems on the hubbard model,” *Phys. Rev. Lett.*, vol. 62, pp. 1201–1204, Mar 1989.
- [36] Y.-W. Son, M. L. Cohen, and S. G. Louie, “Energy gaps in graphene nanoribbons,” *Phys. Rev. Lett.*, vol. 97, p. 216803, Nov 2006.

- [37] J. J. Palacios, J. Fernández-Rossier, L. Brey, and H. A. Fertig, “Electronic and magnetic structure of graphene nanoribbons,” *Semiconductor Science and Technology*, vol. 25, no. 3, p. 033003, 2010.
- [38] E. R. Mucciolo and C. H. Lewenkopf, “Disorder and electronic transport in graphene,” *Journal of Physics: Condensed Matter*, vol. 22, no. 27, p. 273201, 2010.
- [39] S. Das Sarma, S. Adam, E. H. Hwang, and E. Rossi, “Electronic transport in two-dimensional graphene,” *Rev. Mod. Phys.*, vol. 83, pp. 407–470, May 2011.
- [40] S. Roche, N. Leconte, F. Ortmann, A. Lherbier, D. Soriano, and J.-C. Charlier, “Quantum transport in disordered graphene: A theoretical perspective,” *Solid State Communications*, vol. 152, no. 15, pp. 1404 – 1410, 2012. <ce:title>Exploring Graphene, Recent Research Advances</ce:title>.
- [41] G. Schubert and H. Fehske, “Metal-to-insulator transition and electron-hole puddle formation in disordered graphene nanoribbons,” *Phys. Rev. Lett.*, vol. 108, p. 066402, Feb 2012.
- [42] P. W. Anderson, “Absence of diffusion in certain random lattices,” *Phys. Rev.*, vol. 109, pp. 1492–1505, Mar 1958.
- [43] P. A. Lee and T. V. Ramakrishnan, “Disordered electronic systems,” *Rev. Mod. Phys.*, vol. 57, pp. 287–337, Apr 1985.
- [44] G. Schubert, J. Schleede, and H. Fehske, “Anderson disorder in graphene nanoribbons: A local distribution approach,” *Phys. Rev. B*, vol. 79, p. 235116, jun 2009.
- [45] N. Nemec, K. Richter, and G. Cuniberti, “Diffusion and localization in carbon nanotubes and graphene nanoribbons,” *New Journal of Physics*, vol. 10, no. 6, p. 065014, 2008.
- [46] G. Pal, W. Apel, and L. Schweitzer, “Electric transport through circular graphene quantum dots: Presence of disorder,” *Phys. Rev. B*, vol. 84, p. 075446, Aug 2011.
- [47] J. Wurm, A. Rycerz, i. d. I. m. c. Adagideli, M. Wimmer, K. Richter, and H. U. Baranger, “Symmetry classes in graphene quantum dots: Universal spectral statistics, weak localization, and conductance fluctuations,” *Phys. Rev. Lett.*, vol. 102, p. 056806, Feb 2009.
- [48] J. Wurm, K. Richter, and i. d. I. m. c. Adagideli, “Edge effects in graphene nanostructures: Semiclassical theory of spectral fluctuations and quantum transport,” *Phys. Rev. B*, vol. 84, p. 205421, Nov 2011.
- [49] A. Rycerz, “Random matrices and quantum chaos in weakly disordered graphene nanoflakes,” *Phys. Rev. B*, vol. 85, p. 245424, Jun 2012.

- [50] I. Kosztin, B. Faber, and K. Schulten, “Introduction to diffusion monte carlo method,” *American Journal of Physics*, vol. 64, p. 633, 1996.
- [51] W. M. C. Foulkes, L. Mitas, R. J. Needs, and G. Rajagopal, “Quantum monte carlo simulations of solids,” *Rev. Mod. Phys.*, vol. 73, pp. 33–83, Jan 2001.
- [52] J. Thijssen, *Computational Physics*. Cambridge University Press, 2007.
- [53] B. M. Austin, D. Y. Zubarev, and W. A. Lester, “Quantum monte carlo and related approaches,” *Chemical Reviews*, vol. 112, no. 1, pp. 263–288, 2012.
- [54] R. J. Needs, M. D. Towler, N. D. Drummond, and P. L. Ríos, “Continuum variational and diffusion quantum monte carlo calculations,” *Journal of Physics: Condensed Matter*, vol. 22, no. 2, p. 023201, 2010.
- [55] T. Kato, “On the eigenfunctions of many-particle systems in quantum mechanics,” *Communications on Pure and Applied Mathematics*, vol. 10, no. 2, pp. 151–177, 1957.
- [56] M. J. Frisch, G. W. Trucks, H. B. Schlegel, G. E. Scuseria, M. A. Robb, J. R. Cheeseman, G. Scalmani, V. Barone, B. Mennucci, G. A. Petersson, H. Nakatsuji, M. Caricato, X. Li, H. P. Hratchian, A. F. Izmaylov, J. Bloino, G. Zheng, J. L. Sonnenberg, M. Hada, M. Ehara, K. Toyota, R. Fukuda, J. Hasegawa, M. Ishida, T. Nakajima, Y. Honda, O. Kitao, H. Nakai, T. Vreven, J. A. Montgomery, Jr., J. E. Peralta, F. Ogliaro, M. Bearpark, J. J. Heyd, E. Brothers, K. N. Kudin, V. N. Staroverov, R. Kobayashi, J. Normand, K. Raghavachari, A. Rendell, J. C. Burant, S. S. Iyengar, J. Tomasi, M. Cossi, N. Rega, J. M. Millam, M. Klene, J. E. Knox, J. B. Cross, V. Bakken, C. Adamo, J. Jaramillo, R. Gomperts, R. E. Stratmann, O. Yazyev, A. J. Austin, R. Cammi, C. Pomelli, J. W. Ochterski, R. L. Martin, K. Morokuma, V. G. Zakrzewski, G. A. Voth, P. Salvador, J. J. Dannenberg, S. Dapprich, A. D. Daniels, O. Farkas, J. B. Foresman, J. V. Ortiz, J. Cioslowski, and D. J. Fox, “Gaussian 09 Revision A.1.” Gaussian Inc. Wallingford CT 2009.
- [57] O. Voznyy, A. D. Güçlü, P. Potasz, and P. Hawrylak, “Effect of edge reconstruction and passivation on zero-energy states and magnetism in triangular graphene quantum dots with zigzag edges,” *Phys. Rev. B*, vol. 83, p. 165417, Apr 2011.